Motional State Control and Ablation Loading in a Cryogenic Surface-Electrode Trap

Thesis by

Peng Zhou

Supervised by

Chi Zhang and **Dr. Joseba Alonso**

Handed in to

Prof. Dr. Jonathan Home

In Partial Fulfillment of the Requirements

for the Degree of

Master of Science

in

Physics

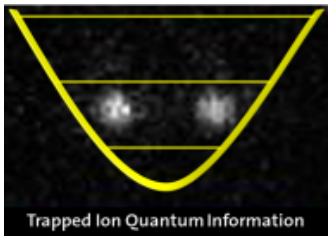

ETH Zürich, Switzerland

October, 2017

To My Mother

Abstract

This Master thesis contains two topics related to a Surface-Electrode Trap (SET) that is kept under 4 Kelvin: motional state control of trapped ion and ablation loading. A SET is a type of ion trap whose all electrodes are in one plane, therefore can be easily fabricated using the well-established photo-lithography technology. The motional state control is further divided into two parts: fast switching and micromotion engineering. The scientific goal of the Fast-Switching experiment is to create non-classical motional state by diabatically manipulating the trapping potential. Despite of the successful creation of large coherent state, our previous attempts to create squeezed state were faced with unexpected observations. In this work the limits for the fast switching control were successfully found and quantitatively analysed, which offers useful insights for the future experiment designs. The study of micromotion is motivated by the possibility of addressing single ions with micromotion sidebands. In this thesis we extended the voltage calculation code for the trapping potential to incorporate the feature of modifying the micromotion quantitatively. Preliminary results are shown for the two-ion experiments. This work lay down the ground work for micromotion-enabled single ion addressing. The Ablation Loading experiment was motivated by the technical tediousness in the current ion loading setup with effusive oven. This all-optical setup offers an alternative using a high-power pulsed laser. Compared to the traditional heated-oven method, this new approach offers several advantages, including shorter loading time better possibilities for loading more than one ion and no heating on the trap.

Acknowledgments

There are many people I am grateful for during the long time of this thesis work and through my master study.

I started to know the TIQI group when I was still a bachelor student in the spring of 2015. My interests in quantum compuationa and simulation lead me to come to ETH for the master studies. One semester later I began to contact Prof. Jonathan Home for the semester project, and it was a great pleasure for me to get the opportunity to work in the group. He was the most involved and comprehensive professor I have ever met. From him, I learnt how to become a real researcher.

The story of this thesis dates back to the summer of year 2016. At that time, I was finishing my semester project on micro-lensed fibre in the TIQI group. Not knowing how to spend the two months of summer break apart from preparing a few exams, I decided to drop by Joseba Alonso's office on a sunny afternoon and ask for a summer project. It happened that he did had a long pended project suitable for my time slot. The project was to design and test an ablation setup for the cryo experiment and the eQual project. Afterwards I began to play around with optical element, align lasers, ask people around for many questions and learn almost everything from scratch. I felt great pleasure to get my hands dirty in the lab. By the end of that summer, I have gained great experiences in real-word experiments at an optics lab. As the summer project is facing with an obstacle related to a suitable fibre, I decided to leave the lab for a while and joined Prof. Andreas Wallraff's lab to gain some knowledge on microwaves.

Joseba didn't forget me. By the time I should decide where and when to do my master thesis a few months later, he contacted me again and asked me to do the thesis with him. I thought it for a while and said yes eventually. I came back to the group and started to work on the thesis in the April of 2017. Since Joseba became busier in this time, my official supervisor has become Chi Zhang. We sit back-to-back in the office and this allows the convenience for me learning from him. We discuss physics and go downstairs to the lab everyday. He teaches me most of the experimental techniques, such as how to run the Ionizer, how to align laser, how to analyse data and so on, step by step. Sometimes during our in-office physics discussion, we ask other members in the office to join us if we cannot figure out the problems ourselves. These include Matteo Marinelli, Karan Mehta and Joseba himself. I quickly gain many theoretical and experimental backgrounds from these seniors.

Within a time of a few weeks, I began to be able to run the Ionizer by myself. Now I start to

ask more questions to whoever in the lab. Since Maciej Malinowski works also in cryo team, I got a lot helps from him when Chi is not available. The person who was outside my team and I bother mostly was Matthew Grau. From time to time, I came to him with all kinds of questions, and his superb knowledge never let me down. Among all the helps from him, it is most worthwhile to mention his guidance on how to use the cryo pump and debugging of the pulsed laser. Besides, I refer to Christoph Fischer for optics, Vlad Negnevitsky for electronics and FPGA programming, Matteo and Christa Flühmann for the setup of lasers and 3D trap, Simon Ragg for the setup of fibre trap. Once in while when Frieder Lindenfelser and Florian Leupold, who were the first PhD generation of the group, came back to the group, I seize the opportunity to get supports from them as well. As the youngest PhD students by the time of this theis, Oliver Wipfli, Robin Oswald, Roland Matt and Chiara Decaroli taught many fresh experiences about the beginning lives of doctoral studies. The afternoon lab works were often interrupted by a joint trip to COOP for an ice-cream or a few kicker games in the common room. During this ten-minute time break and lunch time discussions, I got better chances to know the group members personally and learn more physics.

Outside the helps from these PhD students and postdocs, I attain supports from other people as well. These include Johannes Heinsoo from Andreas Wallraff's group, with whom I sit by change in the same office during my project with Christopher Eichler and Christian Andersen. He put my programming knowledge, especially in Mathematica and Labview, to a new level, and these knowledge remain exceedingly useful for my master thesis. I am also grateful for Andreas Stuker from the mechanical workshop, whose team manufactured the optical shields for my ablation project. At the end of my thesis work, Cagri Oenal joined the group as an electrical engineer. On Tuesday nights when he was available, I obtained more basic knowledge from him about FPGA engineering. And above all, it is worthwhile to meantion Mirjam Bruttin, who is the secretary of group. Her administrative supports greatly ease my life. This thesis also get financial support from the scholarship office in ETH, which mitigates my burdens.

This thesis and my master study cannot be finished without finicial and emotional supports from my friends and family. I am greatly thankful for my mother, Chengying Zhang, to whom I owe the past 23 years already and can never pay the debts off. Our video calls every weekend gave me strength to look ahend and go forward. And finally, a special thank to my girlfriend Mia, for being there with me duing my hard times.

List of Figures

List of Tables

Contents

CHAPTER 1

Introduction and Motivation

1.1 Trapped-Ion Quantum Computation and Simulation

Since the initial fantasy of Richard Feynman on simulating physics with a universal quantum simulator [Feynman82], the research areas on building a quantum computer have gained increasing interests over the last decades. The Shor's algorithm on polynomial-time prime factorisation using quantum computers [Shor95] further indicates that quantum computers can dramatically surpass classical computers in certain problems. In the last 20 years many experimental breakthroughs have been realised in different platforms [Nielsen11], among which trapped ion is one of the leading candidate [Leibfried03; Wineland13].

Nowadays, the ion traps are mainly Paul traps, which include RF electrode and DC electrode to produce a dynamic electric field. The Paul traps are available in different geometries, such as the 3D trap where electrodes are in different layers, and the surface-electrode trap where all electrode are fabricated in one plane. A surface-electrode trap has the advantage of scalability and easier fabrication. In this thesis I perform three experiments on the surface-electrode trap setup in the TIQI group.

1.2 Thesis Structure

The remainder of the thesis covers the setup, theoretical backgrounds, experiments and results in a consistent way, and is structured as following.

Chapter 2 reviews the basic theories for trapping ions in a dynamic electric field and the formalism for treating the ion's motion as a three dimensional quantum harmonic oscillator. Later on, the properties of Calcium ion, which is the species used in our experiments, is discussed, followed by the theory of laser-ion interaction. Chapter 3 briefly gives an overview of the experimental setup, which is the outcome of a PhD generation. In this chapter, only the surface-electrode trap and the laser delivery systems are partially discussed.

Chapters 4–6 contains my main contribution to the experiments and the setup. In Chap. 4 a new bang-bang control experiment is presented. In these experiments we found the current limits of our setup and the overlooked factors in the previous attempts. In Chap. 5 we enhance our experimental capability to control the micromotion of trapped ions. We upgrade our software such that different ions trapped in a same potential can experience different micromo-

tion amplitude. This opens a new possibility for single-ion addressing. Chapter 6 presents a new ion loading scheme with laser ablation, which provides many advantages over our current effusive-oven loading techniques. The successful loading scenarios are illustrated, followed by a systematic study on the ablated atomic plume.

Chapter 7 summaries the results of this thesis and provides an overlook to the future works.

CHAPTER 2

Theoretical Foundations

2.1 Basic Trapology of Quadrupole Ion Trap

In order to trap an ion, or more generally a charged particle, by an electric field, it is necessary to create an electric potential that is confining the charge along all spacial directions. In a source-free electric field, the electric potential satisfies the Laplace's equation:

$$\nabla^2\Phi(\boldsymbol{r},t) = \frac{\partial^2\Phi}{\partial x^2} + \frac{\partial^2\Phi}{\partial y^2} + \frac{\partial^2\Phi}{\partial z^2} = 0, \tag{2.1}$$

where we have expanded the Laplace operator ∇^2 in the Cartesian coordinates. From this equation, we notice that the second order derivatives along three directions cannot be simultaneously all positive. This indicates that it is impossible to confine an ion solely with a static potential. To circumvent this, one way is to use a Paul trap, the Nobel-Prize winning work of Wolfgang Paul [Paul53; Paul90] in 1953, where a radio-frequency (RF) field is introduced to create the radial confinement. Fig. 2.1.a shows a traditional electrode layout of a linear Paul trap in the radial plane. The electrodes are separate rods forming a 3D structure and has demonstrated multiple successful experiments, such as [Clercq16a; Clercq16b; Kienzler15]. In the vicinity of the trap centre, the electric potential can be expressed, to the leading order, as

$$\Phi(\mathbf{r},t) = \frac{1}{2}\sum_{i=x,y,z} u_i r_i^2 + \frac{1}{2}\sum_{i=y,z} v_i r_i^2 \cos\left(\omega_{\text{rf}} t\right), \tag{2.2}$$

where u_i and v_i (in units of V/m^2) represent the potential curvatures that are proportional to the applied voltages and dependent on the trap geometries, and ω_{rf} is the RF frequency. Here and henceforth, the trapping axis is represented as x-axis along which the curvature only comes from the static part $u_x > 0$, and the radial plane refers to the y, z-plane. In order to satisfy the Laplace Equation (2.1), the potential curvatures for a linear Paul trap need to full the conditions:

$$\begin{aligned} u_x &= -u_y - u_z > 0, \\ v_y &= -v_z, \\ v_x &= 0. \end{aligned} \tag{2.3}$$

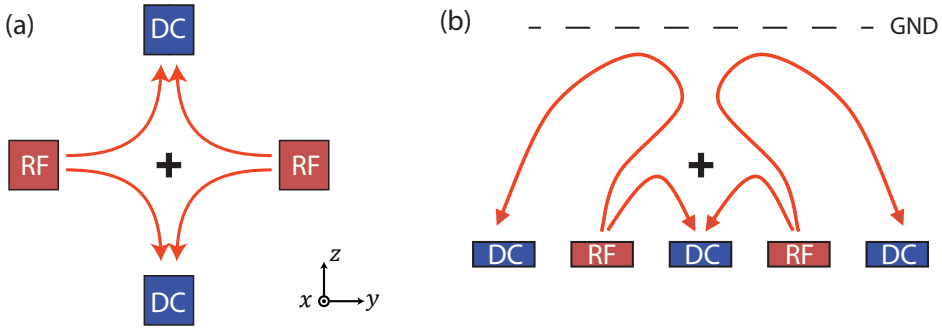

Figure 2.1: Transverse View of Electrode Layouts and Instantaneous Field Lines for Two Linear Paul Traps. (a) A 3D trap. The trapping axis (black cross) is confined by four separate electrode rods, two of which are RF electrodes and the other two are DC electrodes. (b) A surface trap of the "five-wire" layout. All electrodes are constructed within the same plane, above which sits the trapping axis. The dashed line represents a ground plane at infinity.

Fig. 2.1a also shows the instantaneous field lines in the radial plane when the voltage on the RF electrode is higher than the DC voltage. At this instant, the ion is trapped along y-axis and anti-trapped along z-axis, whereas the situation becomes the opposite half of the RF period later. Under the situation where the RF field oscillates much faster than the ion's movement, the ion can be effectively trapped along all three directions.

Despite of its high symmetry, this structure faces difficulty when it comes to constructing in a larger scale that include junctions [Chiaverini05]. A more scalable ion trap structure is a SET, as shown in Fig. 2.1b, where all electrodes are lying within one plane [Chiaverini05]. This layout could be conveniently manufactured by the industrial photo-lithography technology. The ion trap used in this thesis is of this form.

To better understand the trapping potential of the linear Paul traps, we can have a look of at the influence of the RF field to the ion's motion. The total electric potential in Eq. (2.2) can be considered as a summation of a DC part and an RF part, $\Phi = \Phi_{\text{DC}} + \Phi_{\text{RF}}$, with

$$\Phi_{\text{rf}}(\mathbf{r}, t) = \frac{1}{2} V_0 (y^2 - z^2) \cos(\omega_{\text{rf}} t), \tag{2.4}$$

where the conditions (2.3) have been substituted and $V_0 = v_y = -v_z$ is the potential curvature. For an ion with mass m and charge e, its motion in the radial plane due to the RF potential satisfies:

$$\begin{aligned} m\ddot{y} &= -e\frac{\partial \Phi_{\text{rf}}}{\partial y} = -eV_0 y \cos(\omega_{\text{rf}} t), \\ m\ddot{z} &= -e\frac{\partial \Phi_{\text{rf}}}{\partial z} = eV_0 z \cos(\omega_{\text{rf}} t). \end{aligned} \tag{2.5}$$

Due to the inhomogeneity of the electric field amplitude, the ion's trajectory under these equations of motion can be conveniently decomposed into a slowly varying component (y_0, z_0) and

a rapidly varying component (y_1, z_1):

$$\begin{aligned} y &= y_0 + y_1. \\ z &= z_0 + z_1, \end{aligned} \tag{2.6}$$

with $(y_1, z_1) \ll (y_0, z_0)$ and $(y_1', z_1') \gg (y_0', z_0')$. Here $y_0 = \overline{y}$ and $z_0 = \overline{z}$ represent the trajectory of the oscillation centre, where $\overline{(\,)}$ denotes a time average over one period of the RF field, $2\pi/\omega_{\text{rf}}$. In the spirit of Taylor expansion about (y_0, z_0), Eq. (2.5) approximates to

$$\begin{aligned} m\ddot{y}_1 &= -eV_0 y_0 \cos(\omega_{\text{rf}} t), \\ m\ddot{z}_1 &= eV_0 z_0 \cos(\omega_{\text{rf}} t). \end{aligned} \tag{2.7}$$

This can be interpreted as the ion sees a constant RF field amplitude within one oscillation period. And by integrating these equations of motion, we have

$$\begin{aligned} \dot{y}_1 &= -\frac{eV_0 y_0}{m\omega_{\text{rf}}} \sin(\omega_{\text{rf}} t), \\ \dot{z}_1 &= \frac{eV_0 z_0}{m\omega_{\text{rf}}} \sin(\omega_{\text{rf}} t). \end{aligned} \tag{2.8}$$

If we consider its average kinetic energy over one RF oscillating period, we obtain the time-independent *pseudo-potential*,

$$\begin{aligned} \Phi_{\text{ps}}(y_0, z_0) := \langle E_{\text{KE}} \rangle_{(y_0, z_0)} &= \frac{1}{2} m \Big(\langle \dot{y}_1^2 \rangle + \langle \dot{z}_1^2 \rangle \Big) \\ &= \frac{e}{4m{\omega_{\text{rf}}}^2} V_0^2 \Big(y_0^2 + z_0^2 \Big) \\ &= \frac{e}{4m{\omega_{\text{rf}}}^2} |\boldsymbol{\nabla} \Phi_{\text{rf}}(y_0, z_0, 0)|^2. \end{aligned} \tag{2.9}$$

The above approximation is call the *pseudo-potential approximation* and has been found broad applications in other research field such as the plasma physics [Nicholson83]. Under this approximation, we can essentially treat the RF potential as a static potential that governs the slow motion of the ion. The relation between the pseudo-potential and the electric field amplitude in the last line of Eq. (2.9) indicates that the overall effect of the RF field is to drive the ion towards to the weaker field area.

2.2 Classical Treatment of Ion's Motion

Consider an ion with mass m and charge e being trapped in a linear Paul trap with potential (2.2). It satisfies the classical equation of motion (EOM):

$$\frac{\mathrm{d}^2 r_i}{\mathrm{d}t^2} = -\frac{e}{m}\frac{\partial \Phi}{\partial r_i} = -\frac{e}{m}\left[u_i r_i + v_i r_i \cos(\omega_{\text{rf}} t) \right]. \tag{2.10}$$

Along the axial axis, the confinement comes from the DC potential only:

$$\frac{\mathrm{d}^2x}{\mathrm{d}t^2} = -\frac{eu_x}{m}x. \tag{2.11}$$

The motion is simply a harmonic motion with axial frequency $\omega_{\text{ax}} = \sqrt{eu_x/m}$. In the radial plane the EOM's can be written in the form of Mathieu equation,

$$\frac{\mathrm{d}^2r_i}{\mathrm{d}\tau^2} + [a_i - 2q_i\cos(2\tau)]r_i = 0 \qquad (i = y, z), \tag{2.12}$$

with the dimensionless parameters

$$\tau = \frac{\omega_{\text{rf}}t + \pi}{2}, \quad a_i = \frac{4eu_i}{m{\omega_{\text{rf}}}^2}, \quad q_i = \frac{2ev_i}{m{\omega_{\text{rf}}}^2}. \tag{2.13}$$

The stable solutions for Mathieu equation have been well studied [McLachlan64]. In a typical ion trap, we are working in the regime $a_i, q_i^2 \ll 1$. And the solution to Eq. (2.12), to the leading order of q_i, is

$$r_i(t) \approx r_{1i}\cos(\omega_i t + \phi_i)\left[1 + \frac{q_i}{2}\cos(\omega_{\text{rf}}t)\right], \tag{2.14}$$

where

$$\omega_i = \frac{\omega_{\text{rf}}}{2}\sqrt{a_i + \frac{q_i^2}{2}} = \sqrt{\frac{eu_i}{m} + \frac{e^2v_i^2}{2m^2{\omega_{\text{rf}}}^2}} \ll \omega_{\text{rf}} \tag{2.15}$$

is the frequency of the *secular* harmonic motion, and u_{1i} and ϕ_i are its amplitude and phase, respectively, determined by the initial conditions. On top of this, there is an *intrinsic micromotion* with the RF frequency ω_{rf} and a smaller amplitude by a factor of $q_i/2$. This type of micromotion stems from the nature of the oscillating field and remains its presence in an ideal trap. In Chapter 5 I will also discuss the *excess micromotion* that comes from imperfection.

2.3 Trapped Ion as a Quantum Harmonic Oscillator

From Eq. (2.14) we have noticed that the ion follows the motion of a harmonic oscillator. For an ion with sufficiently low kinetic energy, its movement can also be treated quantum mechanically. For later uses, some of the most relevant equations of the quantum harmonic oscillator (QHO) are reviewed in the following.

The *coherent state* is the eigenstate of the destruction operator $\hat{a}$ and can be expressed, in the Fock state basis, as

$$|\alpha\rangle = \exp\left(-\frac{|\alpha|^2}{2}\right)\sum_{k=0}^{\infty}\frac{\alpha^k}{\sqrt{k!}}|k\rangle = \hat{D}(\alpha)|0\rangle, \tag{2.16}$$

where α is a complex number. The second equator denotes that the coherent state can be gen-

erated by applying the *Displacing Operator*,

$$\begin{aligned}\hat{D}(\alpha) &= \exp\left(\alpha\hat{a}^\dagger - \alpha^*\hat{a}\right) \\ &= \exp\left(-|\alpha|^2/2\right)\exp\left(\alpha\hat{a}^\dagger\right)\exp(-\alpha^*\hat{a}),\end{aligned} \tag{2.17}$$

to the vacuum sate. Hence α also illustrates the generally complex displacement in the phase space. Accordingly the coherent state can be considered as the displaced vacuum state. More generally we can apply the displacing operator to any Fock state and obtain the *Displaced Number State* [Nieto97]:

$$\begin{aligned}|\alpha, m\rangle &:= \hat{D}(\alpha)\,|m\rangle \\ &= \exp\left(-\frac{|\alpha|^2}{2}\right)\sum_{k=0}^{\infty}\frac{\alpha^k}{k!}\sum_{j=0}^{m}\frac{(-\alpha^*)^j}{j!}\left[\frac{(m-j+k)!m!}{(m-j)!^2}\right]^{1/2}|m-j+k\rangle\,.\end{aligned} \tag{2.18}$$

For later uses, it is also useful to express the probability distributions of the common sates in the Fock basis $\{|n\rangle\}$ explicitly. These will be useful when performing motional state diagnosis in chapter 4. For a general displaced number state, we have [Boiteux73; Nieto97]

$$\begin{aligned}p_{|\alpha,m\rangle}(n) &= |\langle n|\alpha, m\rangle|^2 \\ &= e^{-|\alpha|^2}n!m!\alpha^{2(m-n)}\left[\sum_{k=\max\{0,n-m\}}^{n}\frac{|\alpha|^{2k}(-1)^k}{k!(m+k-n)!(n-k)!}\right]^2.\end{aligned} \tag{2.19}$$

In the special case of $m = 0$, this is reduced to the probability distribution for coherent state:

$$p_{|\alpha\rangle}(n) = e^{-|\alpha|^2}\frac{|\alpha|^{2n}}{n!}, \tag{2.20}$$

which takes the form of the Poisson distribution with expectation phonon number $\langle n\rangle = |\alpha|^2$. A thermal state is a classical state, whose probability distribution can be expressed as:

$$p_{n_{\text{th}}}(n) = \frac{1}{n_{\text{th}}+1}\left(\frac{n_{\text{th}}}{n_{\text{th}}+1}\right)^n, \tag{2.21}$$

where n_{th} is the average number of phonon and can be related to temperature through:

$$n_{\text{th}} = \frac{1}{e^{\hbar\omega/k_BT}-1}. \tag{2.22}$$

The state becomes ground state when n_{th} = 0. And accordingly, the *displaced thermal state* is given by

$$p_{n_{\text{th}},\alpha}(n) = \sum_{m\geq 0}p_{n_{\text{th}}}(m)p_{|\alpha,m\rangle}(n). \tag{2.23}$$

2.4 Properties of Calcium Atom and Ion

In our setup we work with $^{40}Ca^{+}$, Fig. 2.2 shows its energy levels and Zeeman splitting under our working magnetic field of 4.1 G. The nucleus of ^{40}Ca has no nuclear spin, therefore there is no hyperfine structure. The qubit transition is provided by the quadrupole transition

$$^2S_{1/2}(m_J = -1/2) \leftrightarrow {}^2D_{5/2}(m_J = -5/2), \tag{2.24}$$

which has linewidth of less than 1Hz and is driven by a 729nm laser. For simplicity, these two staes may be simply denoted as $|S\rangle$ and $|D\rangle$ states in the later uses.

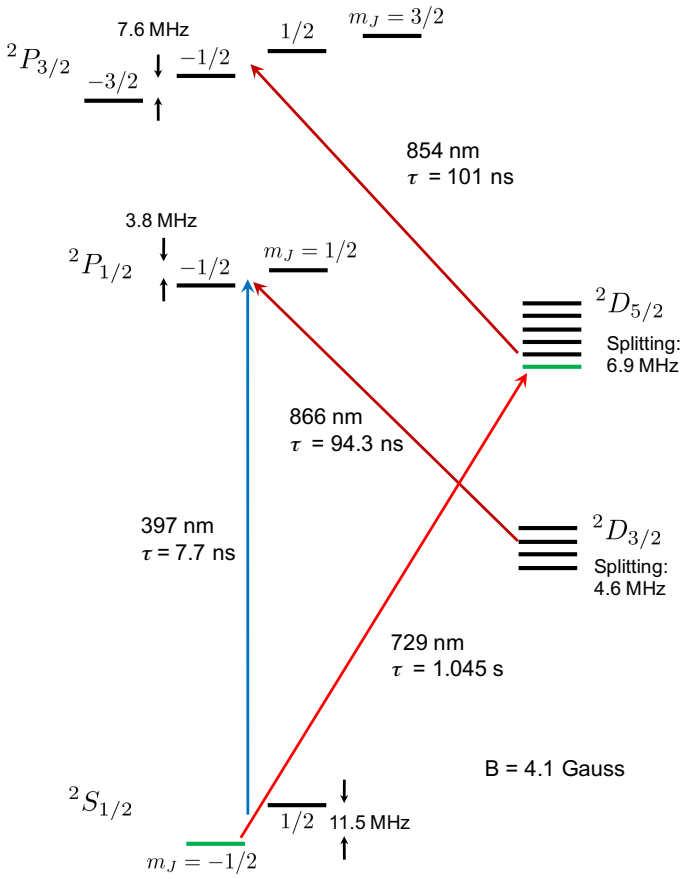

Figure 2.2: $^{40}Ca^{+}$ Energy Levels, together with Zeeman Splitting at magnetic field of 4.1 Gauss and relevant lasers. The two green-coloured levels denote the chosen qubit states in our experiments.

A near-UV 397nm laser drives the dipole transition $^2S_{1/2} \leftrightarrow {}^2P_{1/2}$. This transition allows us to perform laser cooling, spin polarisation, and detection of the qubit state. Due to the branching of the $^2P_{1/2}$ state to the $^2D_{3/2}$ state, we use a 866nm laser to drive the $^2P_{1/2} \leftrightarrow {}^2D_{3/2}$ transition and re-pump the population back to the $^2P_{1/2}$ manifold. Furthermore, a 854nm laser pumps the population from $D_{5/2}$ to $P_{3/2}$, which has lifetime of 7.4ns, in order to increase the repetition rate of the experiments, or perform, for example, reservoir engineering [Kienzler15].

The Calcium ion can be created from Calcium atom through an isotope-selective photoionisation process [Lucas04]. Fig. 2.3 shows the lasers used for ionising neutral ^{40}Ca. First a 423 nm laser excites one electron from its ground state, hence drives the transition $^1S_0 \leftrightarrow {}^1P_1$. Then

a UV 375nm laser excites the electron to continuum

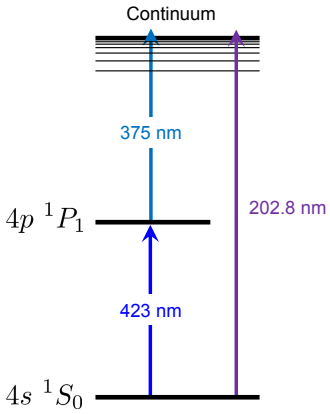

Figure 2.3: Energy Levels of ^{40}Ca Atom, and the ionisation process. (Figure taken from [Lo16].)

2.5 Light-Ion Interaction

In the following I will briefly review some of the most relevant results for describing the coherent interaction between a trapped ion in a hydrogen-like atomic configuration and a monochromatic laser field. These theories will serve as foundations for the data analysis in later chapters. For more detailed review, one may refer to [Leibfried03; Leupold16; Šašura02].

When a trapped ion is interacting with a near-resonant laser field, its internal state can be simplified as a two-level system, $|e\rangle$ and $|g\rangle$, and its motion can be considered as three uncoupled harmonic oscillators under the pseudo-potential approximation. Hence its free Hamiltonian can be written as

$$\hat{H}_0 = \frac{\hbar\omega_a}{2}\hat{\sigma}_z + \sum_j \hbar\omega_{m,j}\hat{a}_j^\dagger\hat{a}_j, \tag{2.25}$$

where ω_a is the atomic transition frequency, $\omega_{m,j}$ is the motional frequency for each of the three harmonic oscillators, and the Pauli matrix $\hat{\sigma}_z$ takes the form $|e\rangle\langle e| - |g\rangle\langle g|$. In this equation the constant terms for the Hamiltonian of harmonic oscillators have been drooped out of convenience.

In our setup, all laser are monochromatic travelling waves whose electric field can be semi-classically described by

$$\begin{aligned}\boldsymbol{E}(t,\hat{\boldsymbol{r}}) &= E_0\boldsymbol{\epsilon}\cos(\omega_L t - \boldsymbol{k}\cdot\hat{\boldsymbol{r}} + \phi)\\ &= \frac{E_0\boldsymbol{\epsilon}}{2}\left[e^{i(\omega_L t-\boldsymbol{k}\cdot\hat{\boldsymbol{r}}+\phi)} + e^{-i(\omega_L t-\boldsymbol{k}\cdot\hat{\boldsymbol{r}}+\phi)}\right],\end{aligned} \tag{2.26}$$

where E_0 is the positive field amplitude, $\boldsymbol{\epsilon}$ is the polarisation unit vector, ω_L the laser frequency, $\boldsymbol{k} = (2\pi/\lambda)\boldsymbol{n}$ the wave vector, $\hat{\boldsymbol{r}}$ the position operator, and ϕ the phase factor. The full Hamiltonian for the hydrogen-like ion is therefore given by

$$\hat{H} = \hat{H}_0 + \hat{H}_1, \tag{2.27}$$

with the interaction term, to the second order, expressed as

$$\hat{H}_1(t) = \frac{eE_0}{2}\left[\hat{\boldsymbol{r}}\cdot\boldsymbol{\epsilon} + \frac{(\hat{\boldsymbol{r}}\cdot\boldsymbol{k})(\hat{\boldsymbol{r}}\cdot\boldsymbol{\epsilon})}{2}\right]e^{-i\left(\omega_L t - \boldsymbol{k}\cdot\hat{\boldsymbol{R}}+\phi\right)} + \text{H.c.}, \tag{2.28}$$

where $\hat{\boldsymbol{R}}$ is the position operator associated with the centre-of-mass (COM) of the ion and $\hat{\boldsymbol{r}}$ the position operator corresponding to the relative position between the valence electron and the COM. From its matrix elements we therefore obtain two types of coupling constants (*on-resonance carrier Rabi frequencies*),

$$\Omega^{\text{DP}} = \frac{eE_0}{\hbar}\langle e|\hat{\boldsymbol{r}}\cdot\boldsymbol{\epsilon}|g\rangle \quad \text{and} \quad \Omega^{\text{QP}} = \frac{eE_0}{2\hbar}\langle e|(\hat{\boldsymbol{r}}\cdot\boldsymbol{k})(\hat{\boldsymbol{r}}\cdot\boldsymbol{\epsilon})|g\rangle\,, \tag{2.29}$$

for dipole transition and quadruple transition, respectively. In the case of $^{40}Ca^{+}$, all the relevant transitions used in our experiment except the qubit transition $^2S_{1/2} \leftrightarrow {}^2D_{5/2}$ are dipole transitions.

By transforming the Hamiltonian in Eq. (2.28) into the interaction picture with

$$\hat{H} = \hat{H}_0 + \hat{H}_1 \qquad \longrightarrow \qquad \hat{H}_{I,1} = \hat{U}_0^\dagger \hat{H}_1 \hat{U}_0, \quad \hat{U}_0 = \exp\left(-\frac{i\hat{H}_0 t}{\hbar}\right), \tag{2.30}$$

and applying the *Rotation Wave Approximation* (RWA) to neglect the fast oscillating terms, we obtain

$$\hat{H}_{I,1} = \frac{\hbar\Omega}{2}\hat{\sigma}_+ e^{-i\delta t}\prod_{j=x,y,z}\exp\left[i\eta_j\left(\hat{\boldsymbol{a}}_j^\dagger e^{i\omega_{m,j}t} + \hat{\boldsymbol{a}}_j e^{-i\omega_{m,j}t}\right)\right] + \text{h.c.}, \tag{2.31}$$

where $\delta = \omega_L - \omega_a$ is the laser detuning relative to the atomic transition, and we have introduced the Lamb-Dicke parameter as

$$\boldsymbol{k}\cdot\hat{\boldsymbol{R}} = \sum_j \eta_j(\hat{\boldsymbol{a}}_j^\dagger + \hat{\boldsymbol{a}}_j), \qquad \eta_j = \frac{2\pi}{\lambda}\sqrt{\frac{\hbar}{2m\omega_{m,j}}}\cos\theta_j, \tag{2.32}$$

where θ_j is the angle between the motional mode and the wave vector.

Working in the Fock state basis of the harmonic oscillator, we can obtain the matrix elements of $\hat{H}_{I,1}$,

$$\langle n_j + s_j|\hat{H}_{I,1}|n_j\rangle = \frac{\hbar\Omega}{2}e^{-i(\delta - s_j\omega_{m,j})t}g_{s_j,n_j}(\eta), \qquad (j = x, y, z) \tag{2.33}$$

with the Frank-Condon coefficients [Wineland79]

$$\begin{aligned} g_{s,n}(\eta) &= \langle n+s|e^{i\eta\left(\hat{a}_j^\dagger + \hat{a}\right)}|n\rangle \\ &= e^{-\eta^2/2}(i\eta)^{|s|}\sqrt{\frac{n_<!}{n_>!}}L_{n_<}^{|s|}\left(\eta^2\right), \end{aligned} \tag{2.34}$$

where $n_< = \min\{n+s, n\}$, $n_> = \max\{n+s, n\}$, and $L_{n_<}^{|s|}(\eta^2)$ is the generalised Laguerre polynomials. When the laser detuning satisfies $\delta = s\omega_m$ for a particular mode, we will drive

the sideband transition $|n\rangle \leftrightarrow |n+s\rangle$ resonantly with Rabi frequency

$$\Omega_{n,s}(\eta) = \Omega g_{s,n}(\eta). \tag{2.35}$$

CHAPTER 3

Experimental Apparatus

This chapter briefly reviews the surface trap used in the later experiments, together with the relevant electric controls (Sec.3.1). Later on the laser delivery system is briefly discussed in Sec.3.2, which also serves as the starting point for the upgrade to ablation loading in chapter 6. For more complete overview of the apparatus, one may refer to [Leupold16].

3.1 Surface-Electrode Trap (SET) and Electronics

Fig. 3.1 shows an image of the trap electrodes, where the electrodes of different functionalities are represented in distinct false colours. These electrodes form a "five-wire" geometry along the radial direction y, as described in Fig. 2.1. Each outer wire is further segmented into 9 DC electrodes, including 2 switchable electrodes and 7 non-switchable electrodes. Together with the middle electrode and an cover plane 2mm above the trap surface, we engineer the voltages applied on these 20 electrodes in order to manipulate the trapping potential.

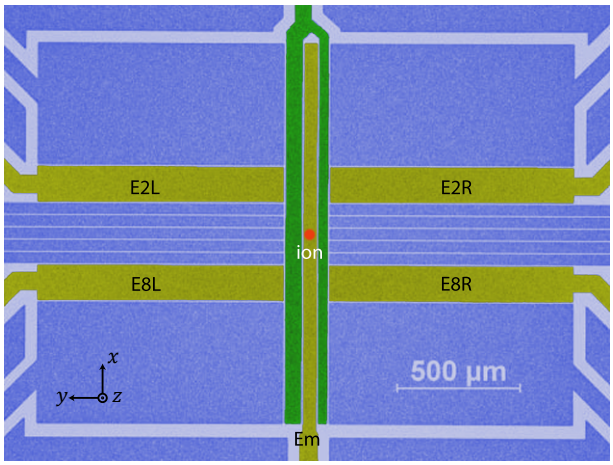

Figure 3.1: False-Colour Image of the Trap Electrode Layout. The five voltage-switchable DC electrodes are coloured in yellow, and labelled as E2L, E2R, E8L, E8R, and Em, respectively. The green coloured electrode stands for the RF electrode, and the rest blue coloured electrodes are non-switchable DC electrodes. An ion is typically trapped at the red-marked position, and around $50\mu m$ above the surface electrodes.

The circuits for controlling the voltages on the DC electrodes are represented in Fig. 3.2. All the voltages are pre-engineered through a python module and stored at the output channels of

a series of 14-bit, ± 10V DACs. These outputs are connected to the CEB throught the vacuum feedthroughs. The three digital controls for each multiplexer is one-to-one connected to the three channels of a digital pulse generator.

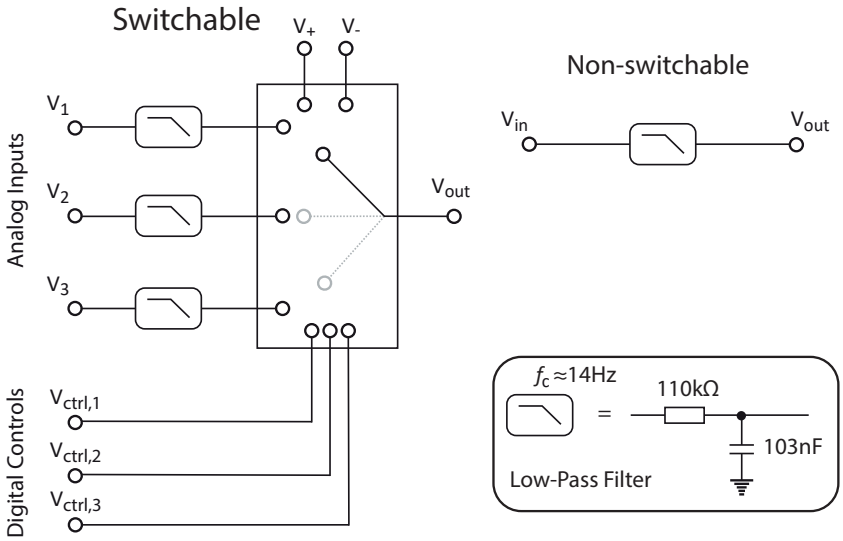

Figure 3.2: Schematics of Voltage controls for switchable and non-switchable electrodes. For switchable electrodes, three

3.2 Laser Delivery

Fig. 3.3 shows the layout of the laser delivery system for the dipole and quadruple transitions in Calcium ion (Fig. 2.2). The trap chip is mounted to face downward and the ion is trapped approximately 50μm below the trap surface. All the laser paths are parallel to the trap chip in order to reduce the light clipping.

The lasers delivered through the bottom viewport are used for laser cooling ($397\,\mathrm{nm}$), repumping ($866\,\mathrm{nm}$ and $854\,\mathrm{nm}$), photon-ionisation ($375\,\mathrm{nm}$ and $423\,\mathrm{nm}$). These laser are coupled to a same photonic-crystal fibre (PCF), and the relevative position of the output of the PCF to the viewport is manually adjusted by translation stages.

The $397\,\mathrm{nm}$ laser on the right is parallel to the magnetic field and σ^--circularly polarised. This laser only couples $S_{1/2}(m_J = 1/2)$ Zeeman level to the $P_{1/2}$ states, and hence pumps all the population from $m_J = 1/2$ to $m_J = -1/2$ after a few cycles.

The $729\,\mathrm{nm}$ lasers are used for coherent interaction with the ion. The 729a beam is at $45°$ to the trap axis, hence couples to both the axial mode and the radial modes of the ion's motion. The 729b beam, on the other hand, is parallel to the trapping axis, therefore only couples to the axial mode.

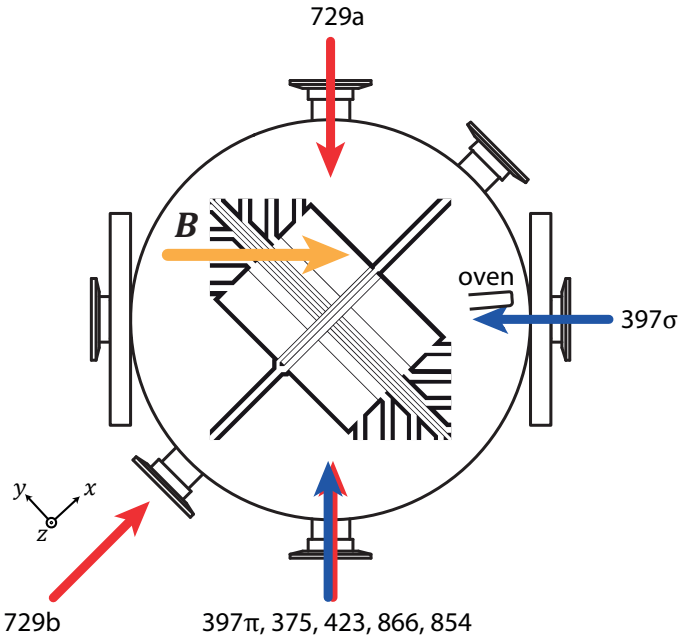

Figure 3.3: Bottom view of the beam delivery layout, relative to the orientations of the surface trap and the effusive oven (not to scale). The big circle in the middle represents the barrel of the cryostat and the six outer components are viewports for light feedthrough and collection. The yellow arrow indicates the direction of the magnetic field, which can be considered as homogeneous in the region of the trap. The red arrows are two 729nm laser beams for coherent manipulation of the qubit transition, with one parallel to the trap axis and the other one at 45°. The five laser beams in the bottom part comes from the same PCF. The 397σ beam in the right part is used for spin polarisation. All the laser beams but 729a are able to couple to both the axial mode and the two radial modes. The small grey box on the right part of the cryostat is the atom oven, which delivers atomic sources approximately perpendicular to the PI lasers. The coordinate system is same as Fig. 3.1, with x-axis being the trapping axis the the y, z-plane being the radial plane.

CHAPTER 4

Fast Switching

One of unique features of our setup was an integration of fast switches with a cryogenic surface trap. Each of the five switchable electrodes chooses one of the three input voltages, through the 3:1 multiplexer, as shown in Fig. 3.2. This allows us to bang-bang control the motional states of the trapped ion and create, for example, a large coherent state that lies beyond the Lamb-Dicke regime [Alonso16]. As a step forward, we have proposed to concatenate the switching cycles to create the squeezed state [Alonso13]. However, in the previous trails we were facing with unexpected problems. This section contains my contributions for figuring out the reasons of these problems and my solutions. In the following sections, I will first provide a more detailed overview of the multiplexer used in our setup and its circuitry. Then the previous observations and problems will be illustrated, followed by possible hypotheses for the reason. We further designed new experiments to verify our hypotheses and finally offer solutions to circumvent them.

4.1 CMOS Analog Switch: a Practical Guide

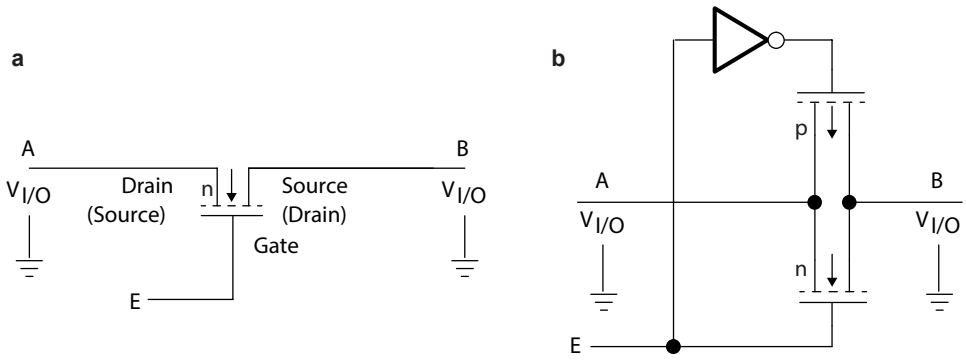

Figure 4.1: Schematics of MOS-FET Switches. (a) A single-FET switch that consists of one n-channel transistor. A and B are two interchangeable I/O ports connected to the drain and source terminals of the transistor, respectively. E is a control (or enable) input that biases the gate voltage. (b) A CMOS switch that consists of a n-channel transistor in parallel with a p-channel transistor. The n-gate and the p-gate are enabled by a high voltage and a low voltage, respectively.

The building block of a three-terminal solid-state switch is a Field Effect Transistor (FET), fabricated with the metal-oxide-semiconductor (MOS) technology. Fig. 4.1.a shows the sim-

plest bidirectional FET switch made of a single n-channel transistor. This switch can conduct signals in either direction when the gate is biased to a high voltage. A more commonly used switch nowadays implements the CMOS technology to incorporate a symmetrical pair of transistors in parallel (Fig. 4.1.b). Apart from its natural advantage of low static power consumption, these switches are featured by their flatter "ON" resistance between drain and source, as the input analog voltages varies. Therefore the CMOS switches are able to operate over a broader voltage range without losing linearity, compared with the single-FET switches.

For the later usage, it is important to mention some of the most relevant switching times here. Fig. 4.2 illustrates four of these times in a switching waveform. More specifically, their meanings are listed as following,

- rise time t_r: the time it takes for the rising edge of the output to take a 10% to 90% transition;
- fall time t_f: the time it takes for the falling edge of the output to take a 90% to 10% transition;
- enable time t_{en}: the propagation delay time to turn on (or to make) a switch;
- disable time t_{dis}: the propagation delay time to turn off (or to break) a switch.

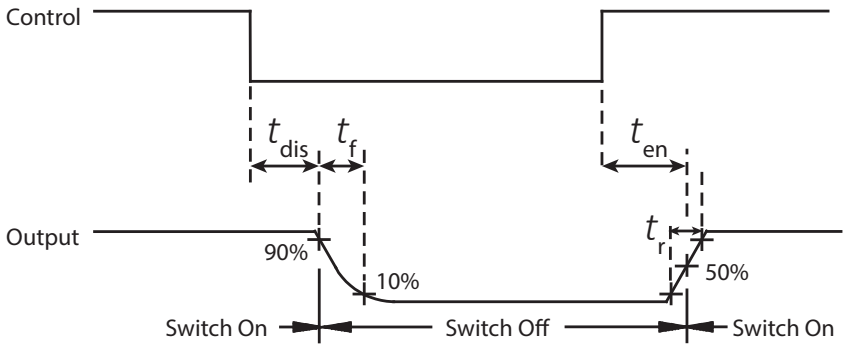

Figure 4.2: Illustration of transition times (t_{r}, t_{f}) and propagation delay times (t_{dis}, t_{en}) in a switching waveform. The upper trace is the control input and the lower trace denotes the output voltage.

The switches used in our experiment are integrated in the CD74HC4066 circuit, manufactured by Texas Instruments®. This device is a member of the 4066 family, which are IC's consisting of four independent SPST switch channels. Each switch can be turned on by a high-level voltage applied to its individual digital control port. Fig. 4.3 shows an image of such a device, together with its functional diagram.

The CD74HC4066 device features a large bandwidth, a low ON resistance, and most relevantly, a wide input voltage range ($V_+ - V_- \leq 9V$, where V_+ and V_- are maximum and minimum input voltages, respectively). The relevant timing specifications are listed in Tab.4.1. In our CEB, we short the output of three such switches to form a 3:1 multiplexer configuration (Fig. 3.2).

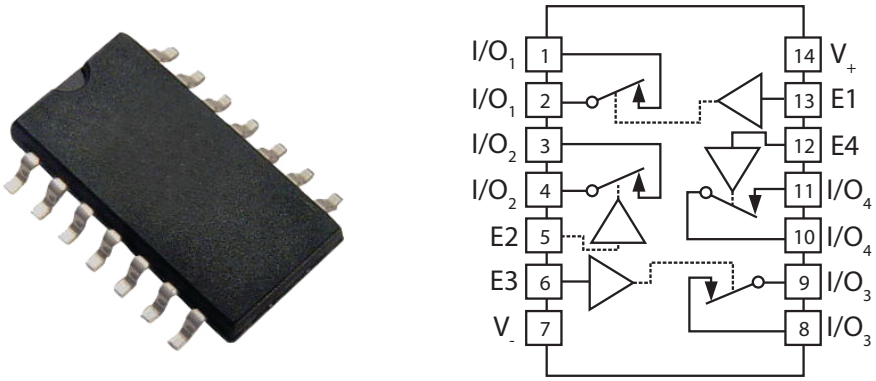

(a) (b)

Figure 4.3: Details of the 4066 IC family. (a) Photo of a surface-mounted device. (b) Top view of the pinout, together with the functional diagram inside. The IC has 14 pins in total, 12 of which are divided for the I/O's and control inputs of the four switches. And the left two are dedicated for the positive and negative supply voltages, V_+ and V_-.

rising time t_r	fall time t_f	enable time t_{en}	disable time t_{dis}
$\leq$ 5 ns	$\leq$ 5 ns	$\leq$ 18 ns	$\leq$ 36 ns

Table 4.1: Timing Specifications of the CD74HC4066 switches. The first two values are taken from the previous measurements under temperature of 4K [Alonso13], while the last two are from the TI spec sheet. The listed values were chosen for positive bias voltage of $9V$ since it's the closest to our working condition.

4.2 Previous Progress and Observations

By engineering the input voltages for different inputs of the multiplexer, we were able to create different trapping potentials for the ion. Prior to the work of this thesis, a handful of attempts have been performed in order to create large squeezed state using two trapping potentials. These trapping potentials have different curvature at the same positions of potential minimum [Alonso16]. At that time, only the one-cycle switching experiments were considered, due to the limit of our pulse generator. Nevertheless, these one-cycle experiments provide a good way to calibrate the two potentials. And once this is operated successfully, it would be straightforward to concatenate the switching cycles by using a more advanced pulse generator.

However, we had encountered with unsolved problems in our previous trials. Fig. 4.4 shows a sequence design for a one-cycle switching experiment. In this experiment, we pre-engineer two voltage sets, Vset_1 and Vset_2, such that the trapping potentials are Pot_1 and Pot_2, respectively. The axial frequencies of Pot_1 and Pot_2 were chosen to be 1MHz and 0.9MHz. These frequencies were lower than our usual axial frequency in order to manifest the fraction of their frequency difference, but they are high enough such that the heating rate, which grows with lower axial frequency, is not limiting our motional coherence. The voltage sets are loaded into appropriate output channels of the DAC box, which are fed to the CEB and can be connected to the trap electrodes through fast switching. We first prepare the ion at the motional ground

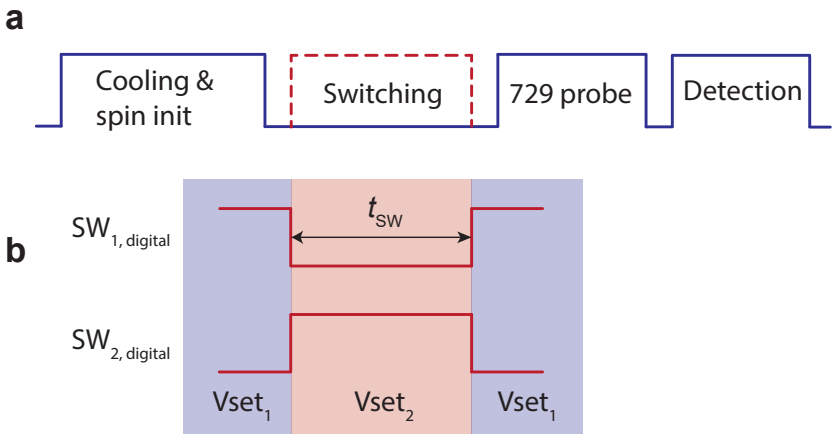

Figure 4.4: The previous experimental sequence for the one-cycle switching experiment. (**a**) The overall sequence. The blue blocks denote the optical controls, and the dashed red lines denotes the optional switching. (**b**) The digital sequences for the switching block in (**a**). $SW_{1,\,digital}$ and $SW_{2,\,digital}$ are the digital signals sent to two switches in each multiplexer. $Vset_1$ and $Vset_2$ are two pre-engineered voltage sets, different shaded areas correspond to the different theoretical voltage sets on the trap electrodes.

state in Pot_1 for the axial mode, then perform a fast switching to change the trapping potential to Pot_2. The ion then freely evolves in Pot_2 for a certain amount of time, t_{SW}, before the potential is switched back to Pot_1. Finally we perform the motional-state diagnosis of the ion, under the original potential Pot_1, by measuring the blue-sideband spectra.

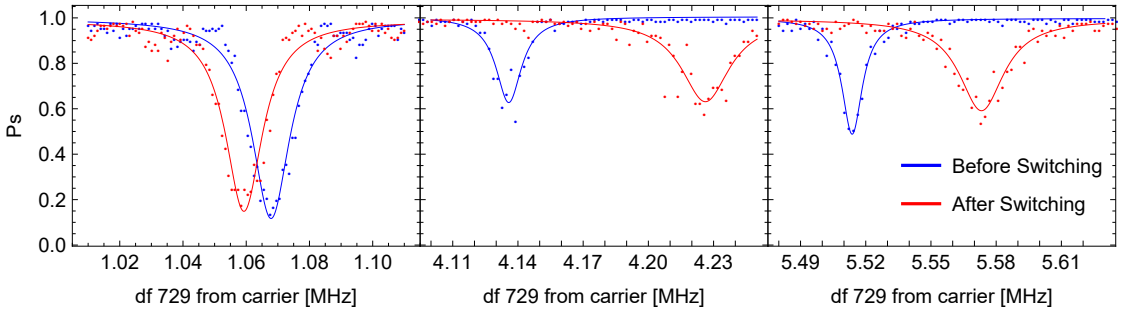

Figure 4.5: Measurements of the first blue sidebands when the switching block in Fig. 4.4.**a** is included (red dots) and excluded (blue dots), together with the Lorentzian fits (lines). The horizontal axis denotes the detuning of 729nm from the carrier transition, which falls in the range of axial sideband (left) and two radial sidebands (middle and right), respectively. The vertical axis denotes the $|S\rangle$ state population after the BSB probe.

Fig. 4.5 explicitly compares first sideband spectra of the sequence with one-cycle switching block and the sequence without. The measurements are fitted with Lorentzian function:

$$L(x; x_0, \Gamma, A, B) = A\frac{(\Gamma/2)^2}{(x - x_0)^2 + (\Gamma/2)^2} + B, \tag{4.1}$$

where x_0 denotes the centre frequency (secular frequency), Γ the Full Width Half Maximum (FWHM), A the scaling factor and B the offset.

Since the ion is always probed in the same potential, i.e. Pot_1, we would expect a trivial result where the secular frequencies for all three modes are not affected by the introduction of the switching block in the sequence. However, From Fig. 4.5 we notice that there were significant changes in both the secular frequencies and the FWHMs. The changes in FWHM could be accounted by the excitation of the ion's motion after evolving in Pot_2 for time t_{SW}. These evaluations can follow the pattern of either coherent state or squeezed state, or a combination of both. The changes in resonant frequency, however, is what we unexpected. These observations indicate that the potential curvature of Pot_1 has changed after one switching cycle, which further means the voltages on the switchable electrodes are different from their original values. And as a result, we cannot concatenate multiple switching cycles without figuring out the reasons.

4.3 Suspected Reasons for the Observations

In this section I will elaborate two hypothesised reasons for the unexpected observations in Fig. 4.5. The first hypothesis was the primary candidate before my joining this work. It lies in the charge exchange between the filter capacitor and loaded electrode that coupled to the ground with a non-zero capacitance. This charge exchange, which decreases as the difference between two capacitances grows, leads to the variation on the filter voltage, hence on the trapping potential. The original direction of this thesis was to mitigate this effect by replace the filter capacitors with the ones with larger capacitance. However, on joining this work, I realised that this effect was insufficient to quantitatively explain the change of secular frequencies in Fig. 4.5. This leads to the second hypothesis that lies in the fundamentals of the multiplexers, and hence a redirection of the thesis.

4.3.1 Reason 1: Non-Zero Capacitance of the Loaded Electrode

When the electrode is connected to the voltage supply, it is referred as a "loaded electrode". Ideally the loaded electrode is floating, indicating that it is far away from any other electrodes and ground. In our real setup, however, the loaded electrode is capacitively coupled to the ground with a tiny capacitance on the order of $C_{el} \sim 10$pF [Alonso13]. Consider a switchable electrode in Fig. 3.2 whose voltage is switched from V_1 to V_2. The charge on this electrode will be changed for an amount of $\Delta Q_{el} = (V_2 - V_1)C_{el}$ during this switching. To compensate this change of charge, it is necessary for the loading electrodes to draw currents from somewhere. Since the low-pass filter in our setup is so strong (14Hz corner frequency, as in Fig. 3.2) such that nearly no current will flow over its resistor within the timescale of switching, the loaded electrodes can only draw the desired currents from the filter capacitors. This leads to the discharging of the filter capacitor, and eventually the discrepancy between the actual voltage on the electrode and the desired voltage.

To alleviate these discharging effect of filter capacitors, we can increase their capacitance

C_{fil} by replacing all filter capacitors and construct a new CEB. According to the relationship between capacitance, change of charge and change of voltage: $C = \Delta Q/\Delta V$, a capacitor with larger capacitance will suffer from less voltage change under the same amount of discharging effect. The resistors in the low-pass filter need to be replaced by the ones with smaller resistance accordingly in order to maintain the corner frequency. A major challenge lying in front is that not all capacitors can work properly under 4K. And typically the larger capacitance, the larger physical size of the capacitor. In order to fix all the capacitors to the CEB with the same size as the current one, careful circuiting is required. Appendix A shows the temperature cycling of larger capacitors, with capacitance one order of magnitude larger than the current ones.

However, to avoid going into a wrong direction, it is necessary to quantitatively examining the significance of this discharging effect. We can obtain the final voltage using the conservation law of the total charges on the filter capacitor for V_2 and loading electrode:

$$V_1 C_{el} + V_2 C_{fil} = V_2'(C_{fil} + C_{el}). \tag{4.2}$$

The l.h.s and r.h.s denote the total charges before and after the switching, respectively, and V_2' represents the final stabilised voltage on both the filter capacitor and the loading electrode. We thus obtain the change of filter capacitor's voltage:

$$V_2' - V_2 = \frac{C_{el}}{C_{el} + C_{fil}}(V_1 - V_2). \tag{4.3}$$

From Eq. (4.3) we notice that, under the ideal situation of $C_{el} = 0$, $V_2' = V_2$ and there is no discharging effect. In our setup we have $C_{el} \sim 10$ pF and $C_{fil} \sim 100$ nF, and as a result $V_2' - V_2 \sim 10^{-4}(V_1 - V_2)$. In our experiment, $V_1 - V_2$ is normally less than 0.1V, which means that $V_2' - V_2$ is smaller than 10μV. This amount of voltage discrepancy is even comparable with the voltage noises on the electrodes, therefore it is suspicious that such small voltage discrepancy could explain the dramatic change of the trapping potential under a single switch cycle, as shown in Fig. 4.5.

To further prove this statement quantitatively, we perform a Finite Element Method (FEM) simulation to investigate the influence of voltage variation to the displacement of potential minimum, and the result is shown in Fig. 4.6. In the simulation, we start from the experimental voltage set Vset_1 in Fig. 4.4. The voltages on the non-switchable electrodes and switchable electrodes are shown in Tables 4.2 and 4.3, respectively. A voltage variation $\mathrm{d}V$ due to the filter capacitor discharge is added on the switchable electrode. We notice that even if we ramp up $\mathrm{d}V$ to $100\mu V$, the potential displacement remains in the sub-nanometer regime, which is smaller than the size of ground state wavefunction and the shift due to electric noises. As a result, the effect due to capacitor discharge can hardly be observed in the bluesideband spectrum.

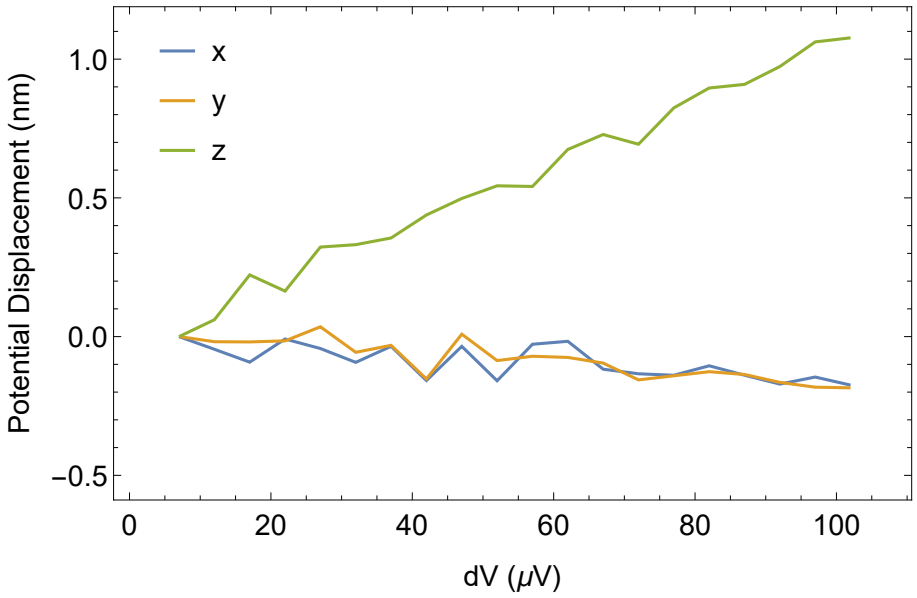

Figure 4.6: FEM simulation result for displacement of potential minimum, as the variations of the voltages on the switchable electrodes. The horizontal axis indicates the discrepancy between the actual voltage and the designed voltage. The three lines represent the displacement along three directions, respectively.

Electrode	E1L	E3L	E4L	E5L	E6L	E7L	E9L
Voltage (V)	0.7283	0.2210	-1.4564	-3.0298	-1.4564	0.2210	0.7283
Electrode	E1R	E3R	E4R	E5R	E6R	E7R	E9R
Voltage (V)	1.3045	4.7540	0.9794	-10	0.9794	4.7539	1.3045

Table 4.2: Voltage inputs on the non-switchable electrodes for the FEM simulation.

Electrode	E2L	E2R	Em	E8L	E8R
Voltage (V)	1.3283	4.7765	-0.5	4.7765	1.3283

Table 4.3: Initial voltages on the switchable electrodes.

4.3.2 Reason 2: Finite Disable and Enable Times

Following the above analysis and the suspicion of whether the non-zero loaded capacitance is the dominant reason, we started to look for other candidates. A more careful examination of the specification sheet of the switch CD74HC4066 indicates that the reason of the charging effect lies in the timing properties of the switches.[1] As indicated on the specification sheet (see table 4.1 for a summary), even though the rising and falling times of the high-speed switch could be as short as 5 ns, there exist two longer and unequal propagation times that limits the speed performance of the switches, the Switch Turn On Delay (t_{en}) and the Switch Turn Off

[1] From the website of Texas Instruments, `www.ti.com/product/CD74HC4066`.

Delay (t_{dis}). These can be explained in the following way: each bidirectional analog switch is controlled by a digital signal. When we want to change the state of the switch, we flip this digital signal. The propagation times t_{en} and t_{dis} denote how long it takes from the flipping in the digital signal to the actual making and breaking of the switch's state, respectively. During these times, the switch can be considered as unaffected and hence the output voltage maintains its original value.

In our experiment sequence (Fig. 4.4), for each multiplexer, we simultaneously disable the switch for Vset_1 and enable the switch for Vset_2. Since the enable time is longer than the disable time, the outputs of the two switches are shorted together during a time window of $t_{\text{en}} - t_{\text{dis}}$, which is on the order of 10ns. This will lead to a direct current flow between the two filter capacitors and eventually the voltages on the filter capacitor are different from the desired values. Apparently, this effect is more significant than the effect described in the last section. This can be further quantitatively verified using the similar analysis for Eq. (4.2) with the conservation law of total charges. We thus obtain the equation for the stabilised voltages,

$$V_1 C_{el} + V_1 C_{fil} + V_2 C_{fil} = V'(2C_{fil} + C_{el}), \tag{4.4}$$

The three terms on the l.h.s denotes the charges on the loading electrode and two filter capacitors before the switching, and the r.h.s denotes the total charges after the switching. V' stands for the stabilised voltage on all the two filter capacitors and the loading electrode. The solution for Eq. (4.4) is

$$V' = \frac{C_{fil}(V_1 + V_2) + C_{el}V_1}{2C_{fil} + C_{el}} \approx \frac{1}{2}(V_1 + V_2), \tag{4.5}$$

where the approximation is valid due to $C_{el} \sim 10^{-4} C_{fil}$. Hence $V' - V_2 \approx (V_1 - V_2)/2$ is four order of magnitude larger than the result in Eq. (4.3). We therefore believe that the effect of non-zero propagation times is more significant than the effect of non-zero loading capacitance.

The above statements lead to a redirection of the work of this thesis. Before replacing the capacitors with the ones with larger capacitance, we should see whether we can mitigate or even eliminate the effect of potential change in Fig. 4.5 when the finite propagation times are taken into account

4.4 Experiments and Results

Now that we have identified the dominate possible reason for the variation of secular frequencies, as shown in Fig. 4.5, we designed two sets of experiments where the non-zero propagation times are taken into account, which would be the main contents of this section. The first kind of experiment is a straightforward upgrade to the sequence in Fig. 4.4 in order to decrease the shorting time of two capacitors, hence to mitigate the variation of secular frequencies. Following the desired observation, we performed a more systematic analysis in order to precisely calibrate the propagation times for each multiplexer. These results lay down the overlooked foundations for further fast-switching experiments.

4.4.1 Break-Before-Make Switching

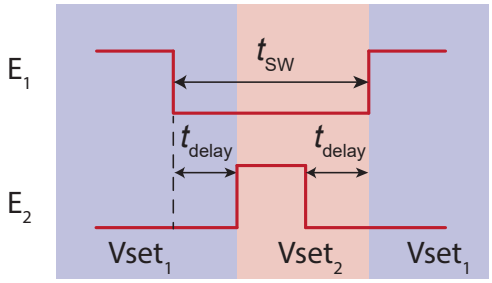

Figure 4.7: New designed digital control sequences for the Break-Before-Make (BBM) switching experiments. In comparison with Fig. 4.5.**b**, t_{delay} is the delay time between breaking switch 1 and making switch 2. The shaded colours indicate the expected voltage sets on the switchable electrodes in the situation of zero propagation times.

To decrease the direct charge exchange between filter capacitors due to finite switch disable and enable times, we designed a new experimental sequence where we break one switch before making another (Fig. 4.7). In comparison with the previous sequence, a "delay time" is introduced between the falling edges and the rising edges of the different enable inputs. If we gradually increase t_{delay}, we would expect the effect of channel overlap being mitigated.

We performed the same experiment as in Fig. 4.4.a and measured the axial secular frequencies when the new switching part is absent and present. The final results are shown in Fig. 4.8. We can notice that the difference in axial frequencies indeed decreases as the delay time increasing, and finally approaches 0 when delay time is around 30ns. These data is coincided with the specifications in Tab.4.1 and confirms our hypothesis that the overlap effect can be mitigated by increasing delay time. We also further increased the delay time, but lose ion every time for t_{delay} larger than around 34 ns. In order to figure out the reason for losing ions, and calibrate more precisely t_{en} and t_{dis}, we performed more systematic studies, as shown in the next section.

In Fig. 4.8.b and Fig. 4.8.c we have also shown explicitly the axial bluesideband spectra for $t_{\text{delay}} = 0$ns and $t_{\text{delay}} = 30$ns. Apart from the observation that the secular frequencies are closer for larger t_{delay}, we still observe the increasing of FWHM. This indicates that the ion is

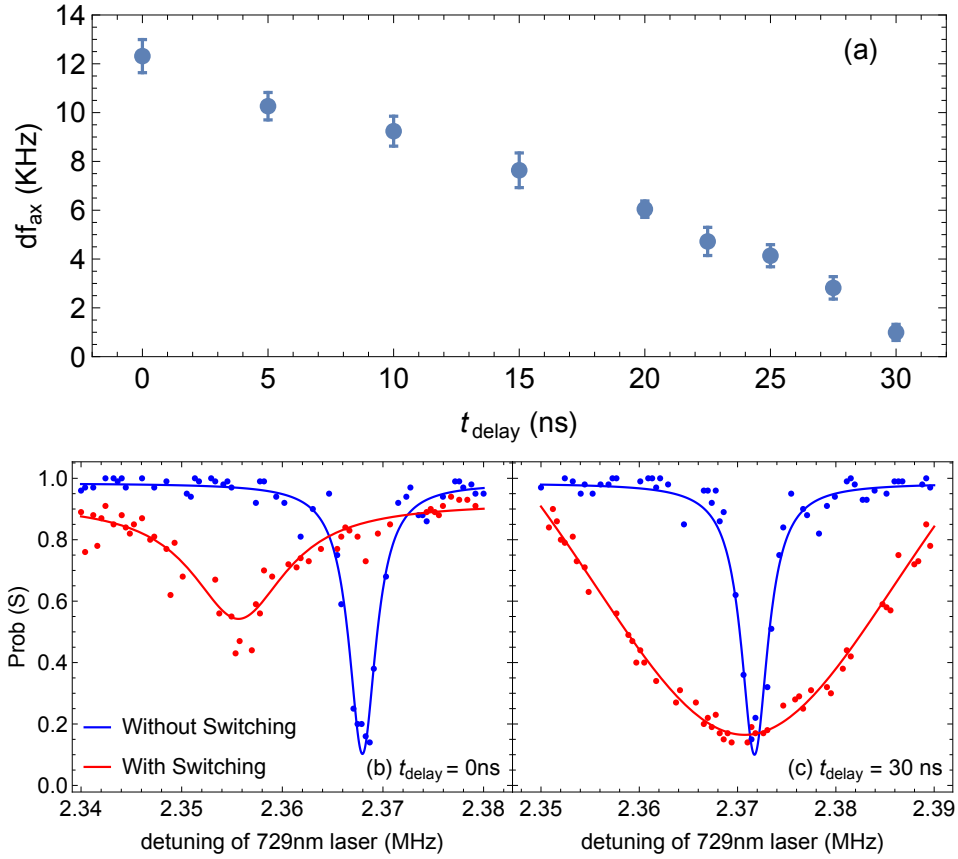

Figure 4.8: Results of BBM switching. (a) The difference of the axial secular frequencies between non-switched sequence and switched sequence. As the delay time increases, this difference approximates to zero gradually. The error bars denote 3σ, i.e. 99.7% confidence level, where σ is the stand error. (b) and (c) are two direct comparisons where the delay times are 0ns and 30ns, respectively. The blue and red dots are probabilities to find the ion in S state, for the non-switched sequence and switched sequence, and the solid lines are Lorentzian fittings. $\mathrm{d}f_{\mathrm{ax}}$ in (a) is obtained from the difference between the two fitted centre frequencies.

no longer in the ground state of Pot_1 after being evolved in Pot_2.

4.4.2 Systematic Analyses and Diagnosis of Ion Loss

The former measurements indicate that a switching sequence compensating for the finite propagation times indeed improves our control over the trap voltages. However, there are two practical questions to be answered:

1) What is the reason for losing ion every time when $t_{\text{delay}} > 30$ ns in sequence Fig. 4.7?
2) How large should we set t_{delay} in the experimental sequence for creating vacuum squeezed state?

In order to answer these questions, we performed a systematic study of the switches by designing a very simple experiment referred as Off-Time Switching, as shown in Fig. 4.9.a. In this figure, we also illustrates the expected voltage on the switchable electrode where the non-zero propagation times are taken into account. In this experiment, we remove the enabling signals for the second switches in each multiplexer. Each multiplexer is effectively used as an SPST switch. This would allow us to tell whether the ion loss is due to the disabling of SW_2 or is related to the enabling of SW_1. Furthermore, we were suspecting that the ion loss might result from malfunctioning of one of the five multiplexers. To find this out, we sent this sequence to one multiplexer each time. In the hardware level, this is realised by reconnecting the circuitry outside the cryostat such that only one enabling port of the multiplexers is connected to the DPG, while the other four is connected to constant voltage source.

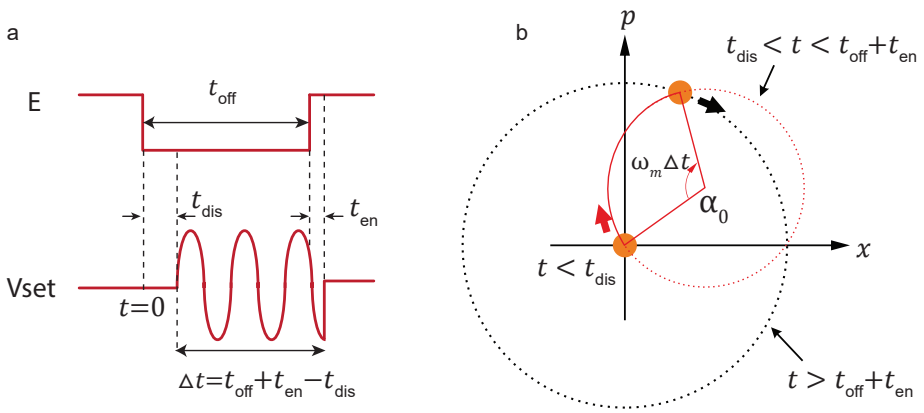

Figure 4.9: (a) Control Sequence for Off-Time Switching. Only one voltage set Vset_1 is used. The digital control for the switch is at low voltage for time t_{off}. When the switch is disabled completely, the loading electrode becomes floating and capacitively coupled to the RF electrode. The lower panel shows the actual voltage on the loading electrode. (b) Phase-space interpretation of the ions's motion. The ion sits in the ground state before $t_{\text{off}} = t_{\text{dis}}$. Afterwards it becomes $|-\alpha_0\rangle$ in the displaced potential and evolves for time Δt. Finally the potential changes back, leaving the ion's state given by Eq. (4.6).

In the beginning of the experiment, the digital control for the switch is set to HIGH and the switchable electrode has the desired value from Vset. The ion is prepared in the ground state of this potential. The digital control is then flipped to LOW for a time of t_{off} before flipped back to HIGH. Afterwards we analyse the ion's motional state by performing the Rabi oscillations on the first bluesideband.

As we scan over the off time t_{off}, the voltage on the examined switchable electrode is expected to fell into different regimes:

1) When $t_{\text{off}} < t_{\text{dis}} - t_{\text{en}}$, the switch is effectively unbroken and therefore the voltage remains unchanged.
2) When $t_{\text{off}} > t_{\text{dis}} - t_{\text{en}}$, for the beginning time of t_{dis} the switch is unbroken and the voltage remains the unchanged. Later on the switch is broken and the switchable electrode becomes floating. However, since it is capacitively coupled to the RF electrode and no longer RF grounded, the voltage on this electrode will oscillate with the RF frequency, with the mean value same as the Vset. This will last for a period of $\Delta t = t_{\text{off}} - t_{\text{dis}} + t_{\text{en}}$. Afterwards the electrode is reconnected to the voltage supply and the voltage changes back to the original value. This scenario is illustrated in Fig. 4.9.a.

We first perform the experiment for the switchable electrode E2L, as labelled in Fig. 3.1, and the result is shown in Fig. 4.10.a. For each t_{off}, we probe the axial motional state by performing the Rabi oscillation on the first blue sideband. From this figure we notice that for $t_{\text{off}} \leq 30$ns, the Rabi oscillations remain the same, indicating that the ion remains at the ground state. This demonstrates that the connection between the electrode to its voltage source is not yet broken and the electrode voltages remain their original values, as illustrated above in the first regime.

As t_{off} increases further, this connection is physically broken. Since the electrode is not connected to a second voltage source after losing its connection to the first source, we expected the ion's motional state unaffected by the disconnection before running the experiments. The reason is that there is no DC path from the tested electrode to other electrodes. The voltage on this electrode will remain constant if there is no other voltage source forcing it to change. However we notice that for $t_{\text{off}} > 30$ns, the Rabi oscillations start to run faster than the ground-state oscillation and show an periodic behaviour with a period of around 400ns. This is a signature of the ion's motion being excited during the disconnection time. This made us to realise that the switchable electrode is no longer RF grounded if it is detached from its filter capacitor (Fig. 3.2). This overlooked fact rules out the simple fix to the propagation delay issue by designing the BBM sequence in Fig. 4.7 with t_{delay} longer than the maximum of t_{dis} among all multiplexers.

Similar as analysis in the creation of coherent state with bang-bang control [Alonso16], The excitation of ion's motion can be depicted in the phase space in Fig. 4.9.b. During the time of Δt when the switchable electrode E2L is not RF grounded, the Paul trap is no longer linear since the symmetry along x-axis is broken. The pseudo-potential is therefore modified in this period. This can be as a combination of effects of a momentum kick to the ion and a displacement of trap potential saddle point by amount of x_d. Generally speaking, there should also be phase-space displacement in the radial plane, but this will not be the topic of the following since we were not probing the radial modes. Effectively in the phase space, the ground state of the new trapping potential is displaced by a complex number α_0 and the ion's state can be considered as $|-\alpha_0\rangle$. After this time, the potential changes back to its original form, and the ion becomes a coherent state (or more rigorously speaking, a displaced thermal state with a small mean thermal

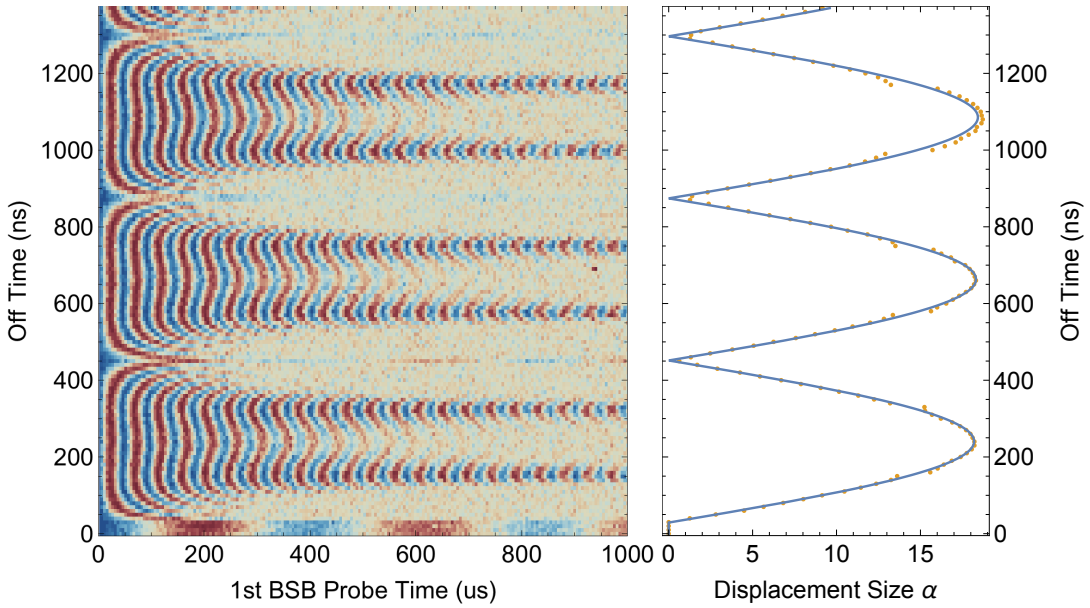

Figure 4.10: Off-Time Switching for Electrode E2L. *left panel:* Rabi Oscillations on the 1st blue sideband for different switching off time. The vertical axis indicates the off time t_{off} and each horizontal line is the corresponding Rabi oscillation. The colour represents the probability of finding the ion in $|S\rangle$ state. *right panel*: Coherent State Lobes. Each dot denotes a fitted result from the corresponding row in the left panel, and the solid line is a fitting according to Eq. (4.6).

population) with size:

$$|\alpha| = |\alpha_0|\sqrt{2[1-\cos(\omega_m \Delta t)]}, \tag{4.6}$$

where $\Delta t = t_{\text{off}} - t_{\text{dis}} + t_{\text{en}}$ is the evolving time in the displaced potential, and ω_m is the secular frequency.

In order to analyse this coherent state, we first fit the Rabi oscillation for the non-displaced state at $t_{\text{off}} = 0$ns with the probability of finding the ion in $|S\rangle$ state (from Eq. 2.33):

$$P_S(t_p) = \frac{1}{2}\sum_{n\geq 0} p_{n_{\text{th}}}(n)\Big[1 + e^{-\gamma t_p}\cos(\Omega_{n,n+1}t_p)\Big], \tag{4.7}$$

where $p_{n_{\text{th}}}(n)$ is the probability distribution of a displaced thermal state in Fock state basis (Eq. 2.23), t_p is the probing time, γ is the decay rate, and $\Omega_{n,n+1}$ is the Rabi frequency for driving the sideband $|n\rangle \leftrightarrow |n+1\rangle$ given by Eq. (2.35):

$$\begin{aligned}\Omega_{n,n+1}(\eta) &= \Omega g_{s,1}(\eta) \\ &= \Omega e^{-\eta^2/2}\eta\sqrt{\frac{n!}{(n+1)!}}L_n^1(\eta^2).\end{aligned} \tag{4.8}$$

In this experiment, we used the 729b laser beam, which is parallel to the trapping axis. Hence the Lamb-Dicke parameter is the largest among all geometrical configurations:

$$\eta = \frac{2\pi}{\lambda_{729}}\sqrt{\frac{\hbar}{2M\omega_m}} \approx 0.063. \tag{4.9}$$

Plugging this value into Eq. (4.7), we obtain the fitting result, as shown shown in Fig. 4.11 and Tab.4.4.

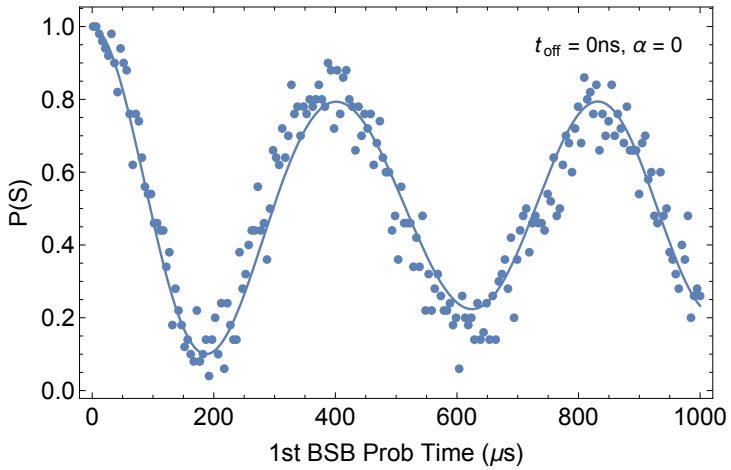

Figure 4.11: Rabi oscillation in the 1st blue sideband for $t_{\text{off}} = 0\,\text{ns}$, together with fitting to Eq. (4.7)

Thermal mean quantum number n_{th}	0.20(3)
Decoherence rate γ	$2.01(25)$ ms^{-1}
Carrier-transition Rabi frequency Ω	$2\pi \times 38.62(11)$ KHz

Table 4.4: Fitting parameters for the non-displaced state at $t_{\text{off}} = 0$.

Taking the fitting results in Tab.4.4 as the input values, we are able to extract the displacement size for each state in the regime of $t_{\text{off}} \gtrsim 30$ ns from the probability function

$$P_S(t_p) = \frac{1}{2}\sum_{n\geq 0} p_{n_{\text{th}},\alpha}(n)\Big[1 + e^{-\gamma t_p}\cos(\Omega_{n,n+1}t_p)\Big], \tag{4.10}$$

where $p_{n_{\text{th}},\alpha}(n)$ is given by Eqs. (2.23) and (2.19). Despite that α is the only fitting parameter in this equation, the numerical analysis is less straightforward, due to the complicated form of $p_{n_{\text{th}},\alpha}(n)$. The detailed fitting procedure is shown in Appendix B. Fig. 4.13 shows three fitted examples with different off time and displacement size.

The displacement sizes for all off times are shown in Fig. 4.10.b, as a direction comparison with the 2D plot. This plot illustrates a signature of coherent lobes, indicating that we have created large coherent state by bang-bang control, similar as the the procedure in [Alonso16]. We fit the values in Fig. 4.10.b according to Eq. (4.6) and obtain $|\alpha_0| = 9.07(4)$ and $t_{\text{dis}} - t_{\text{en}} = 29.0(7)$ ns.

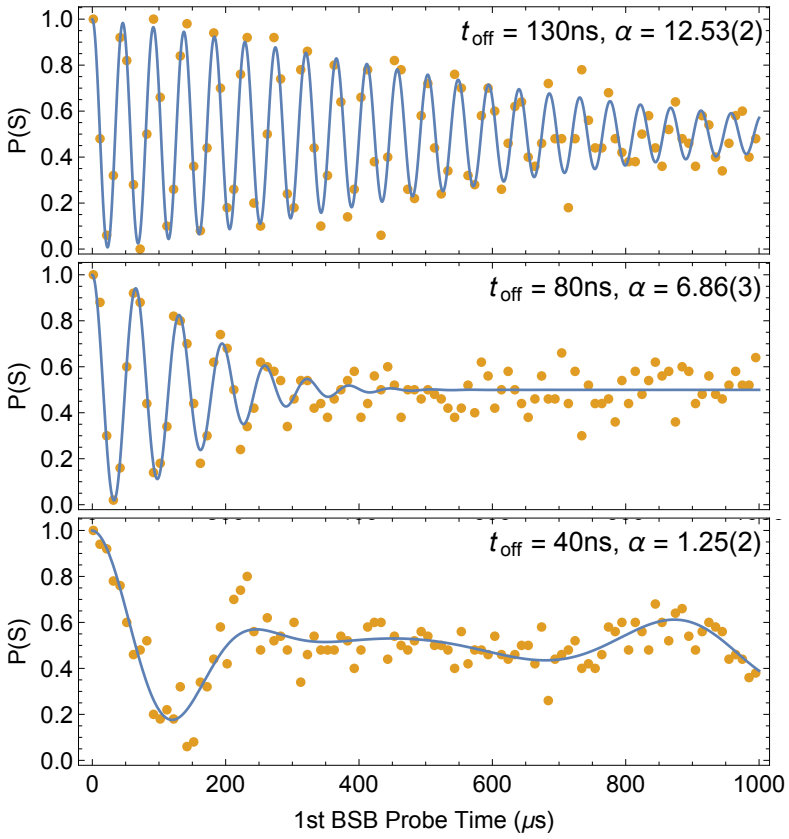

Figure 4.12: Rabi oscillations in the 1st blue sideband for displaced states of different sizes. From bottom to top, each panel corresponds to a different off time in Fig. 4.10. The yellow dots denote the measurement data and the blue curves are fittings according to Eq. (4.7).

Following the study on electrode E2L, we performed similar experiments on all of the four outer switchable electrode, and the results are shown in Fig. 4.13. For each electrode, only the first 500ns are represented, which contains a full period of coherent state evolution.

From these figures we observes very similar behaviours for the four outer switchable electrodes. For the first $30\,\mathrm{ns}$, the Rabi oscillators remain unchanged. As the off times increases beyong $30\,\mathrm{ns}$, a signature of displaced state shows up. These confirms our suspicion that the propagation delay time is a universal property for all the switches used in our experiment.

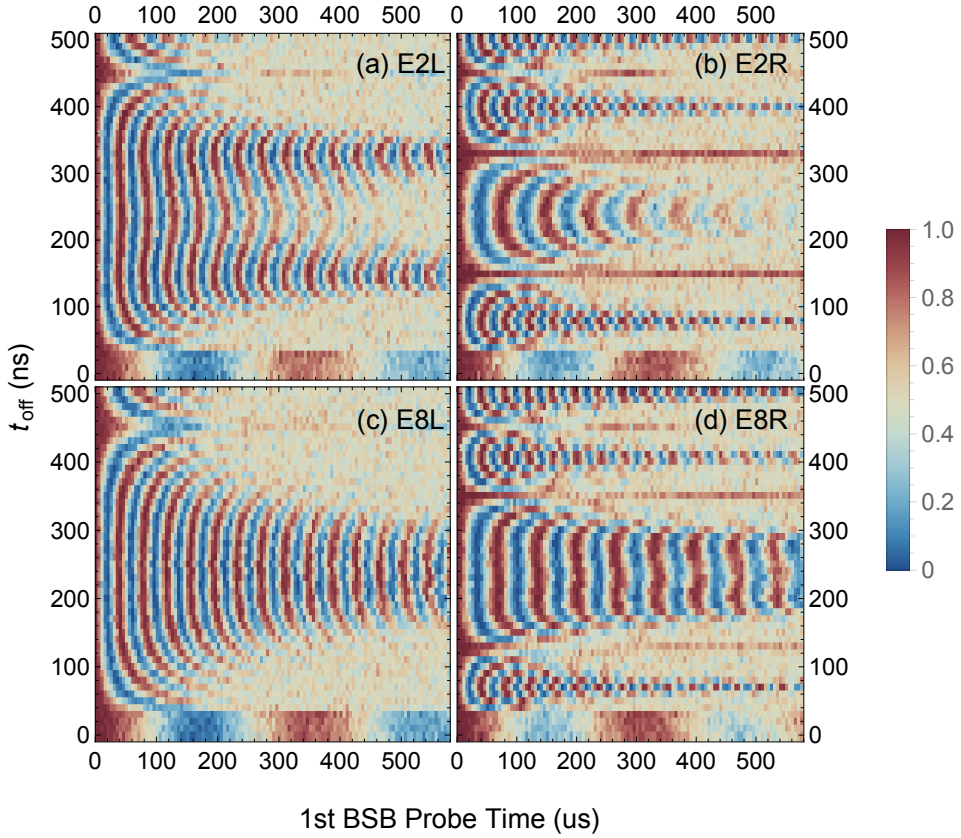

Figure 4.13: Individual Off-Time Switching for the four outer switchable electrodes, (**a**) E2L, (**b**) E2R, (**c**) E8L, (**d**) E8R.

Comparing the two rows in Fig. 4.13, we notice that E2L is similar to E8L and E2R is similar to E8R. This is consistent with our electrode geometry, which exhibits a reflection symmetry in the x direction. Further, the dissimilarity between the two columns results from the fact that the two fingers of the RF electrode have different thickness (Fig. 3.1). As the ion's position is closer to the electrode on the right side, the voltage changes in E2R and E8R have more dramatic influence on the displacement of the trapping potential. This can be further confirmed in Fig. 4.14, where the first coherent state lobes are obtained for each electrode, using the similar process for Fig. 4.10b.

Apart from the experiment on outer switchable electrode, we also performed the same procedure on the inner electrode Em (Fig. 3.1). The results show the same trivial behaviour on the first 30ns off time, indicating that the switch is not broken. However, as soon as we further increase t_{off}, we lose the ion every time by running the same experimental sequence. This can be explained from our analysis above. When the middle electrode Em is disconnected from any

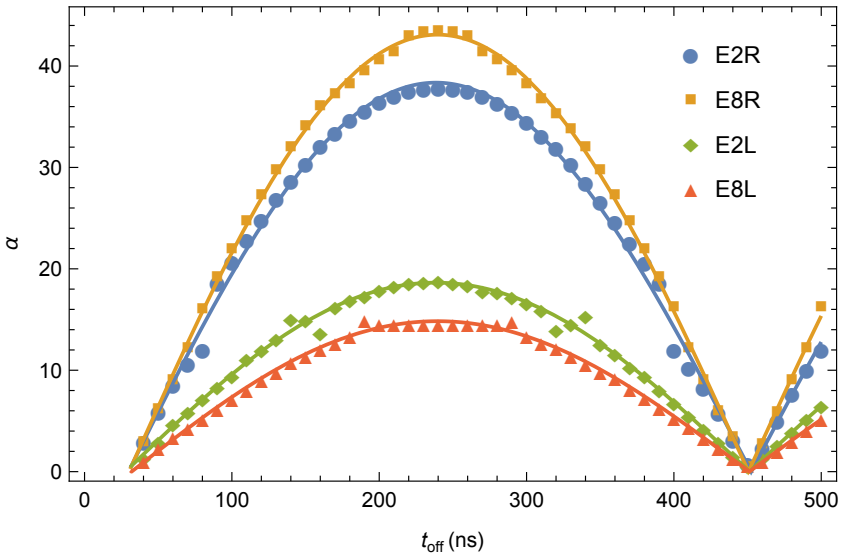

Figure 4.14: Displacement Size analysis for the four subfigure in Fig. 4.13

voltage supply, it is not RF grounded and becomes an RF electrode (Fig. 4.9.a). However, from Fig. 2.1 we can notice that a DC electrode is crucial in forming a stable quadrupole trap in the five-wire geometry. When $t_{\text{off}} > 30\text{s}$, a stable trap does not exist. Therefore the ion is kicked out every time.

4.5 Conclusions and Further Steps

In this chapter a long-standing issue in the fast switching experiment has been solved. The experiments prior to the work of this chapter were faced with observations that the voltages on the switchable electrodes are changed after one switching cycle. It was believed that these changes result from the charge exchange between the filter capacitor and the non-zero capacitance formed by the loaded electrode and ground. In this chapter, a more quantitative analysis illustrates that this is not the dominating reason. Instead, a new hypothesis related to the finite propagation times were proposed after a careful reading of the specification sheet of the multiplexer.

We designed a new Break-Before-Make (BBM) switching sequence and confirmed that by inserting a delay time t_{delay} between breaking the first switch and making the second switch, the voltage changes could be dramatically mitigated. Afterwards, a series of off-time switching on individual switchable electrode were performed, demonstrating a creation of displaced state when the examined electrode is disconnected from DC voltage source. This was explained by the fact that the switchable electrode becomes a RF electrode during the time of floating. The propagation time and the size of the displaced state were calibrated for each switch. Furthermore, the reason for ion losing in the BBM switching for large t_{delay} was found to be the non-existence of a stable quadrupole trap when Em becomes a RF electrode.

These experiments enable new insights for further designing of switching experiments. In order to create a squeezed vacuum state by alternating the trapping potential between two predesigned potentials, it is important to make sure the potentials remain unchanged during the

experiments. To do this, the delay time t_{delay} has to be precisely the difference between switch enable time and disable time, $t_{\text{dis}} - t_{\text{en}}$, which is about 30ns. If $t_{\text{delay}} < t_{\text{dis}} - t_{\text{en}}$, the two switches are overlapped and the their corresponding filter capacitors are shorted. If $t_{\text{delay}} > t_{\text{dis}} - t_{\text{en}}$, the switchable electrode will become a RF electrode during some time, causing a complex displacement on the ion's motional state. However, a precise equality between t_{delay} and $t_{\text{dis}} - t_{\text{en}}$ is not feasible in practice. This rules out the scheme to create a squeezed vacuum state by fast switching.

Nerveless, the calibration of propagation delay times might be useful in experiments with more tolerance on potential change. One example would be the fast transport of ion, where three trapping potentials are necessary, with different saddle point positions.

CHAPTER 5

Micromotion Engineering

5.1 Intrinsic and Excess Micromotion

In Eqs. (2.12) – (2.15) we have shown the origin of *intrinsic micromotion* with the classical treatment of ion's motion. Intrinsic micromotion occurs due to the presence of the RF drive, and it still persists for an ideally engineered DC potential whose saddle point in the radial plane coincides with the pseudo-potential null. In practice, there is also *excess micromotion* when the saddle point of the DC potential is misaligned with the pseudo-potential null. This could be due to un-calibrated stray electric fields or deliberate engineering [Leupold16]. One common cause for stray fields is the coating of electrodes with ions or electrons from the oven and photo-ionisation process. Under these situations, the EOM Eq. (2.12) becomes inhomogeneous:

$$\frac{\mathrm{d}^2 r_i}{\mathrm{d}\tau^2} + [a_i - 2q_i \cos(2\tau)]r_i = f_i(\tau), \qquad (i = y, z). \tag{5.1}$$

In the simplest case where an additional homogeneous stray field $\mathbf{E}^{\mathrm{s}} = \{E^{\mathrm{s}}{}_x, E^{\mathrm{s}}{}_y, E^{\mathrm{s}}{}_z\}$ is added to the desired field, the r.h.s. takes the time-independent form $f_i = 4eE_i^s/m{\omega_{\mathrm{rf}}}^2$. To the leading orders of a_i and q_i, the solution becomes [Berkeland98]:

$$r_i(t) \approx [r_{0,i} + r_{1,i}\cos(\omega_i t + \phi_i)]\left[1 + \frac{q_i}{2}\cos(\omega_{\mathrm{rf}} t)\right], \tag{5.2}$$

where

$$r_{0,i} \approx \frac{Q E^{\mathrm{s}}{}_i}{m\omega_i^2} \tag{5.3}$$

is the shifted average position. Comparing with Eq. (2.14), we now have an additional term $r_{0,i}q_i\cos(\omega_{\mathrm{rf}}t)/2$ also oscillating with the RF frequency. This is the excess micromotion. In the remaining of this chapter, we focus solely on excess micromotion. In addition to the classical treatment of micromotion, a fully quantum mechanical development for both single ion and a trapped-ion crystal is also available [Bermudez17].

When an ion with non-zero excess micromotion interacting with a laser field, it experiences a laser phase being modulated at the RF frequency [Leupold16]. We can therefore make the

following substitution to Eq. (2.26):

$$e^{-i\omega_L t} \longrightarrow e^{-i\left[\omega_L t + \boldsymbol{k}\cdot\boldsymbol{a}\sin\left(\omega_{\mathrm{rf}} t\right)\right]} = e^{-i\omega_L t}\sum_{j=-\infty}^{j=+\infty} J_j(\beta) e^{i\omega_{\mathrm{rf}} t}, \tag{5.4}$$

where $\boldsymbol{a}$ is the amplitude of excess micromotion and $\beta = \boldsymbol{k}\cdot\boldsymbol{a}$ denotes the modulation index. We have expanded the equation to the Bessel functions of the first kind $J_j(\beta)$. For non-zero and increasing β, the strength for carrier transition ($j = 0$) decreases and the strength for micromotion-sideband transition ($j \neq 0$) increases. This can be observed in both dipole transition (e.g. the 397 nm $^2\mathrm{S}_{1/2} \leftrightarrow {}^2\mathrm{P}_{1/2}$ transition) and quadruple transition (e.g. the 729 nm qubit transition). Fig. 5.1 shows the observation of micromotion when we deliberately misalign the DC potential saddle point and the pseudo-potential null in the y direction.

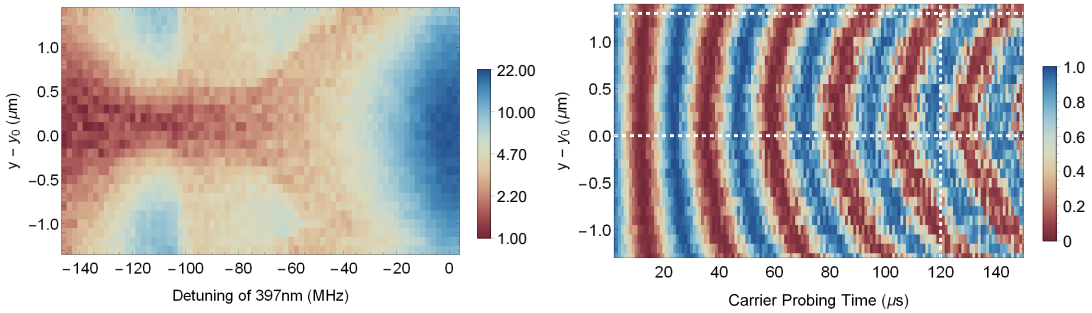

Figure 5.1: Modulation of Light-Matter interactions due to excess micromotion. The vertical axes denote the position of the engineered potential minimum, in y-direction, relative to the pseudo-potential null (y_0). (*left*) Observation of the micromotion sidebands in the fluorescence spectrum. The horizontal axis represents the detuning of the reference cavity for the 397nm laser, relative to the $^2\mathrm{S}_{1/2} \leftrightarrow {}^2\mathrm{P}_{1/2}$ transition resonance. The fluorescence counts are shown in the logarithmic scale. (*right*) Micromotion's influence on Rabi oscillations in the carrier transition. After a probing time of $120\mu s$ (vertical dashed line), the oscillations at the two horizontal dashed lines are out of phase by π.

In our experiment, $\omega_{\mathrm{rf}} \approx 2\pi \times 95\,\mathrm{MHz}$, which lies beyond the bandwidth of the acousto-optic modulators (AOMs) installed in the beams lines. However, for the 397 nm transition, we are able to increase the laser detuning to this range by changing the length of the reference cavity. The existence of excess micromotion is manifested in the appearance of the fluorescence peak at $\omega_a - \omega_{\mathrm{rf}}$. For the 729 nm qubit transition, such direct observation is not yet available. But we are able to observe the decrease of carrier-transition Rabi frequency as the increasing of the excess micromotion. This motivates the possibility for micromotion-enabled single ion addressing, which is the main topic in the next section.

5.2 Excess Micromotion for Single Ion Addressing

Single qubit addressing plays an important role in the operation of a general quantum computer. In a chain of trapped ions , the distance between nearest neighbours is around 5 micrometers. To manipulate the state of individual ions, one way is to focus the laser to a beam size smaller than ions' interspacing, which is on the order of a few micrometers. For a Gaussian beam, a tightly focused beam spot size inevitably comes with the price of larger divergence. For a typical SET application, a rather complicated optics is required in order to avoid beam clipping of the diverging beam on the trap surface.

Since the Rabi frequency is modulated by the existence of the excess micromotion, we can engineer the trapping potential such that different ions in a ion chain experiences different micromotion. This opens up an alternative possibility of single ion operation using a global laser beam. The protocol examined below is similar to the one used in [Navon13].

5.2.1 Engineering Off-Diagonal Terms in the Hessian Matrix

In all of the above experiments, the electrode voltages are engineered such that the total trapping potential satisfies

$$\begin{aligned} \boldsymbol{E}(\boldsymbol{r}_{\mathrm{MMC}}) &= \begin{pmatrix} 0 & 0 & 0 \end{pmatrix}, \\ \mathbf{H}(\boldsymbol{r}_{\mathrm{MMC}}) &= \frac{M}{e} \begin{pmatrix} {\omega_{\mathrm{ax}}}^2 & 0 & 0 \\ 0 & \times & \times \\ 0 & \times & \times \end{pmatrix}, \end{aligned} \tag{5.5}$$

where $\boldsymbol{E}$ is the electric field with each term given by the first-order derivative of the total potential $E_i = \partial\Phi/\partial r_i$, $\mathbf{H}$ is the Hessian matrix with each term given by the second-order derivation $\mathbf{H}_{ij} = \partial^2\Phi/\partial r_i \partial r_j$, M the mass of Calcium ion and e is the electric charge. The matrix elements marked by "$\times$" in $\mathbf{H}$ are not constrained in our voltage optimisation routine. Both the electric field and the Hessian matrix are evaluated at a micromotion compensated position $\boldsymbol{r}_{\mathrm{MMC}} = \boldsymbol{r}_{\mathrm{PS}} + \Delta\boldsymbol{r}$ with $\boldsymbol{r}_{\mathrm{PS}}$ being the position of pseudo-potential null and $\Delta\boldsymbol{r}$ accounts for the position shifts due to the stray field. Once the constraints in Eq. (5.5) are satisfied, we have engineered a trapping potential with trapping frequency $\omega_a x$ in the axial direction and lying parallel to the pseudo-potential null. If multiple ions are trapped inside this potential, they will experience no excess micromotion ideally.

In order to introduce a spatially variant micromotion into the trapping potential, we engineer a perturbation voltage set satisfying

$$\mathbf{H}_1(\boldsymbol{r}_{\mathrm{MMC}}) = \begin{pmatrix} 0 & \mathbf{H}_{yx} & \mathbf{H}_{zx} \\ \mathbf{H}_{yx} & \times & \times \\ \mathbf{H}_{zx} & \times & \times \end{pmatrix}. \tag{5.6}$$

More details on how to engineer the perturbation voltages numerically can be found in Appendix C.

5.2.2 Preliminary Results on Two-Ion Experiments

Following our previous discussions on engineering the spatially variant micromotion amplitude for an ion chain, Fig. 5.2 shows the preliminary results on a chain consisting of two Calcium ions. The two figures compares the Rabi oscillations for zero off-diagonal terms and non-zero off-diagonal terms in the Hessian Matrix. We notice that when $\text{Hess}_{yx} = 0$, the two ions oscillate with similar Rabi frequencies, and there is no approach to distinguish them. For $\text{Hess}_{yx} = 40\,\text{MV}/\text{m}^2$, however, there is a clear beat signal, which manifested the difference of the carrier Rabi frequencies of the two ions.

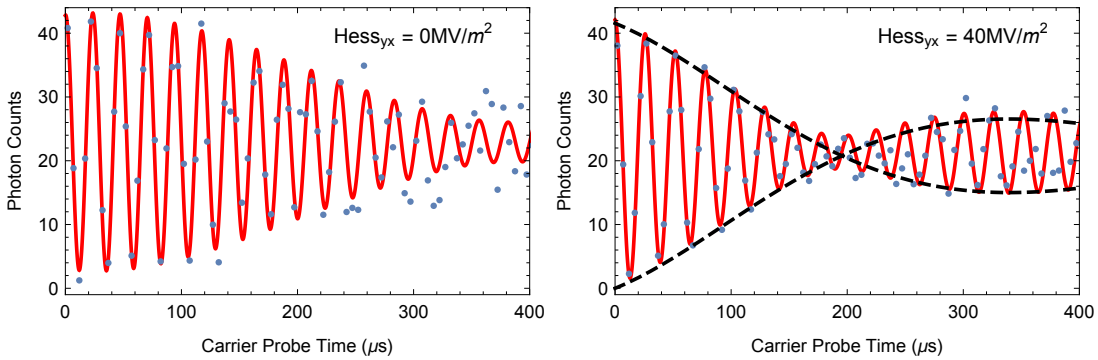

Figure 5.2: Rabi Oscillations for Two-Ion Experiments. The horizontal axes denote the probing time with resonant $729\,\text{nm}$ laser, and the vertical axes are the total fluorescence photon counts in a detection widow of $200\mu s$. (*left*) The off-diagonal terms in the Hessian matrix are zero. The two ions experience the same micromotion modulation. (*right*) The off-diagonal terms in the Hessian matrix are engineered to be $\text{Hess}_{yx} = 40\,\text{MV}/\text{m}^2$ and $\text{Hess}_{zx} = 0$ in the possition of the pseudo-potential null, such that the two ions have different micromotion amplitudes. The red solid lines are fittings according to Eq. 5.7 and the black dashed lines are the profiles for the beat signal.

We fit the results with

$$N_{\text{photon}}(t) = A \sum_{i=1,2} \frac{1}{2}\Big[1 + e^{-\gamma_i t}\cos(\Omega_i t)\Big], \tag{5.7}$$

where i denotes the index for different ions, Ω_i is the ion-dependent Rabi frequency, A is a scaling factor, and γ_i accounts for the decoherence of the internal state. The fitting results give $\Omega_1 = 2\pi \times 39.70(5)$ kHz and $\Omega_2 = 2\pi \times 37.14(8)$ kHz. This gives rise to the beat frequency

$$\Omega_{\text{beat}} = \frac{1}{2}|\Omega_1 - \Omega_2| = 2\pi \times 1.28(5)\text{kHz}. \tag{5.8}$$

At the node of the beat signal, the two rabi oscillations interfere completely destructively since one ion is in the $|S\rangle$ state while the other is in the $|D\rangle$ state. This determines the gate time for

single ion addressing:

$$T_g = \frac{\pi/2}{\Omega_{\text{beat}}} = 195(7)\mu s. \tag{5.9}$$

More generally, for two ions start from an arbitrary product state:

$$(a_1 |S\rangle + b_1 |D\rangle) \otimes (a_2 |S\rangle + b_2 |D\rangle), \tag{5.10}$$

this protocol allow us to perform a π rotation on one ion while the state of the other ion remains unchanged. The eventual product state becomes:

$$(a_1 |S\rangle + b_1 |D\rangle) \otimes (a_2 |D\rangle + b_2 |S\rangle). \tag{5.11}$$

5.3 Conclusions and Future Work

In this chapter we laid down foundational works on excess micromotion engineering. This opens a new path for addressing individual ions in a trapped-ion crystal. The basic scheme is that by tilting the trapping axis around the micromotion compensated axis, we are able to create a spatially variant micromotion modulation to the Rabi frequency. When the Rabi oscillators for two ions with different excess micromotions are out of phase by π, they can be distinguished from each other. We performed a preliminary 2-ion experiment, exhibiting a gate time for individual readout of around 200 μs.

In our setup, the radio frequency $\omega_{\text{rf}} \approx 2\pi \times 95\,\text{MHz}$ is larger the the bandwidth of the AOMs for the 729 beam lines. In the future if we replace the AOMs by the ones with larger bandwidth, we would be able to drive the micromotion sideband directly, similar to the approach in [Nazarov03]. This has a potential of decreased single-ion gate time, and hence better fidelity. Furthermore, there will be possibilities for micromotion-enabled entangling gate [Bermudez17].

CHAPTER 6

Ablation Loading

In the majority of the state-of-art trapped-ion labs, ions are loaded from an effusive oven that is thermally connected to a temperature controller and consists of the suitable metal sample. Typically, the oven is a few centimetres away from the loading zone of the trap, and when heated, a cloud of neutral atoms would form and travel around. Depending on the atom species, the oven needs to be heated to different temperatures, in order to account for the different surface binding energies. As the atom cloud passes through the loading zone, some atoms can be ionised by the photo-ionisation lasers, resulting in ions. The ions, if having sufficiently low kinetic energies compared to the trapping depth, can be captured by the electric field. While the electric force is conservative, the ion motion can be excited by interacting with background gas or anomalous heating [Deslaurier06; Turchette00]. Therefore the cooling lasers are normally turned on in order to keep the ions loaded,

As a standard approach stemmed from the cold atom community, the effusive oven method can be conveniently set up in a room-temperature experiment. However, when it comes to a cryogenic architecture, whose temperature gradients across different components have to be taken into consideration, this method becomes far more laborious. The most influential difference is that when the oven is heated, the temperature inside the cryostat will increase as well and some liquid helium will blow up, hence raising the dewar pressure. The vaporisation of liquid helium leads to the possibility of misalignment between the cryostat and the lasers. We have to re-align the lasers accordingly in order to compensate for this influence. Consequently the loading time in a cryogenic experiment usually is much longer than that in the room-temperature experiments. Furthermore, even if some ions are successfully trapped, we have to wait for some time until the whole system cools down.

Instead of heating the whole chunk of the metal sample to collect the atom cloud, an alternative approach is to illuminate a high intensity laser to locally heat a focused spot on the the surface of the metal. This high laser flux is able to strip off, or ablate, the materials from the solid surface. Depending on the laser intensity, different regimes need to be considered [Leibrandt07; Hendricks07]. This process has been used widely in manufacturing and chemical analysis. In the trapped ion community, the ablation loading setup usually refers to a nanosecond pulsed laser with energy in the range from hundreds of μJ to a few mJ.

In the rest of this section, I will first briefly describe our current effusive oven setup. Based on this, the updated setup that encompasses a pulsed Nd:YAG laser will be introduced. In

the optical setup, we first tried to couple the pulsed laser in to a fibre in order to utilise its convenience. We later on discontinued this approach because of no appropriate fibre available and set up the optics in free space. The successful ablation loading events using this setup will be discussed. And finally we performed systematic studies on the velocity distribution of the neutral atom plume. This study provides us with some hints for identifying better ablation loading parameters.

6.1 Current Setup with Effusive Oven

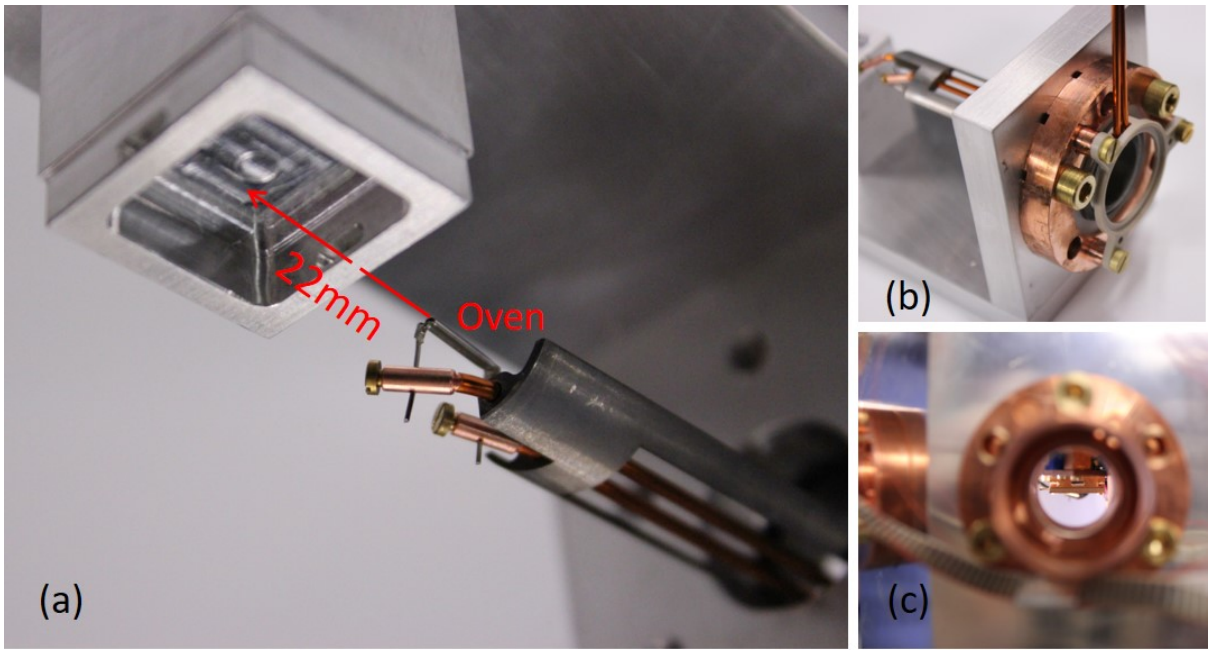

Figure 6.1: Images of the effusive oven setup. (a) The relative position of the oven and the trap. The socket is where the trap chip is placed, and its centre is the position to trap the ion. The oven tube is electrically connected to a thermal heater. Once heated, the atom cloud flies for around $22\,\mathrm{mm}$ before being caught by the trap. (c) Image of two electric wires from the oven. (d) View of the oven and trap holder from the opposite viewport (shown as the left viewport in Fig. 3.3).

The layout of our effusive oven setup is shown in Fig. 6.1. The oven is a stainless steel tube[1] with an inner diameter (ID) of $1.06\,\mathrm{mm}$ and wall thickness of $0.1\,\mathrm{mm}$. The ends of the oven tube are bent and mechanically connected to copper wires. These copper wires enable current flow through the oven tube, hence heating the Calcium granule inside. A typical setting for thermal controller is around $4\,\mathrm{A}$ and $1\,\mathrm{V}$ [Leupold16]. After being heated, evaporated calcium atoms fly for an distance of around $22\,\mathrm{mm}$ before arriving at the trapping region. The PI and cooling lasers, which propagate almost perpendicularly to the flying direction of the atoms (Fig. 3.3), allow ionisation of the atom and loading of the ion.

The effusive oven method has many disadvantages in practice. In our experiment, the typical loading time using the effusive over varies from a few minutes to more than 20 minutes. During this time, we constantly heat the oven, leading to an overall heating of the UHV chamber. We

[1] 89935K66 from McMaster-Carr.

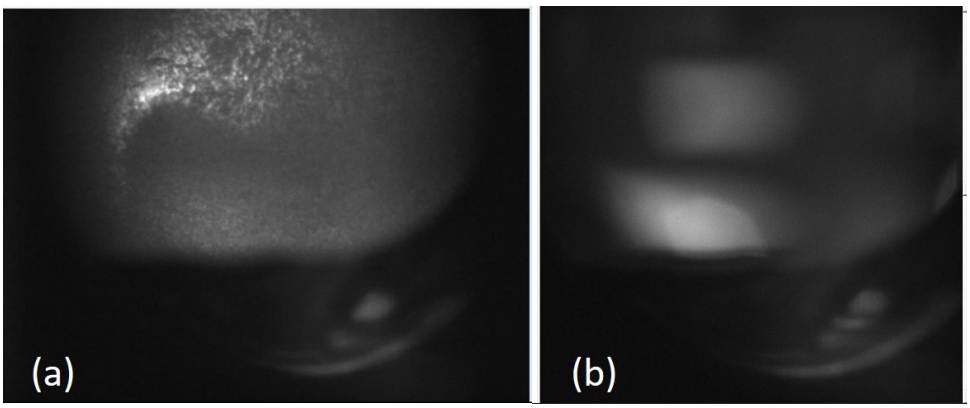

Figure 6.2: Images of coating on the viewport. The viewport is chosen to be the one on the left of Fig. 3.3 with no laser feedthrough. (a) A clear view of the coating on the inner window. (b) Image taken for the same position after the cryostat being warmed up, during which the coating has disappeared.

normally stops the heating if the temperature on the CEB increases beyond 20K. This amount of heating causes many unwanted changes in the experimental environment. One of the major effects is the evaporation of liquid Helium and increase of the pressure of the Helium dewar. This leads to an overall displacement in the vertical direction of the UHV chamber, and as a result, the lasers will be clipped by the holes in the Faraday cage or by the trap edge. This clipping oscillates at the frequency of the remote motor of the cryostat, which is $1.4\,\mathrm{Hz}$, as can be seen by the $397\,\mathrm{nm}$ fluorescence counts. It severely influences our diagnosis of the ion's state. Therefore each time when an ion is loaded, we have to wait for some time until the system is cooled down.

The setup is neither the best option for loading multiple ions, since the total loading time is so long such that multiple ions can hardly be stably trapped. In the single ion addressing experiment in Chapter 5, we only managed to load two ions a few times.

Another drawback of effusive oven lies in the coating of the viewport. After the oven being heated for a long time, a large atomic aloud would be created. As the UHV chamber cools down, there will be residue atoms accumulated on the window of the chamber (Fig. 6.2). This viewport coating will result in a decrease in the laser transmission, which influence the accuracy of experiments. The coating can be removed by warming up the whole system to room temperature. However, it takes about one week to do a full temperature cycle for our cryostat. During the time of this thesis, the cryostat was warmed up every three months.

6.2 Upgrade the Setup

In order to bypass the disadvantages related to the effusive oven method, we intend to upgrade ion loading scheme to an all-optical method. The Calcium atom is created from single laser pulses of a high-intensity pulsed laser. Similar setups have been realised for a 3D trap with Ca^+ [Hendricks07] and a 3D trap with both Ca^+ and Al^+ [Guggemos15]. The scheme was also shown in the room-temperature surface-electrode trap for Be^+ [Wahnschaff16]. The realisation

for a cryogenic surface-electrode trap, however, would be more difficult due to a combination of small trapping depth and the complexity of the cryogenic setup. In this section, a practical guide on how to operate the pulsed laser is first illustrated. Later on we describe two approaches for the ablation laser setup, one with a fibre and the other one without. Eventually we had to adapt the approach without the fibre due to the high intensity of the laser pulse that exceeds the damage thresholds. The successful ion loading results were demonstrated afterwards. Finally the creation of the neutral atom plume from the laser pulse was systematically analysed.

6.2.1 Pulsed Laser: a Practical Guide

The pulsed laser used in our setup is a Minilite II Nd:YAG laser from Continuum®. This model offers tunable repetition rate 1-15 Hz with a typical pulse width 5-7 ns. We operate at the fundamental wavelength $1064\,\mathrm{nm}$, since the cost is the lowest and we care pulse energy more than the wavelength. However, the second harmonic can be easily generated by inserting a doubling crystal inside the laser head and obtain wavelength 532nm. This wavelength falls in the regime of visible light, which would be easier to align than $1064\,\mathrm{nm}$.

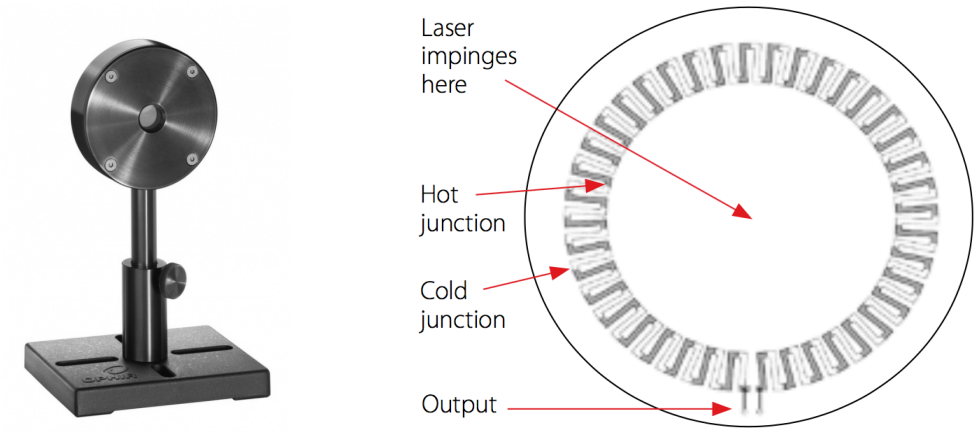

(a) (b)

Figure 6.3: Working Principles of Thermal Sensors. (a) Image of a thermal sensor. (b) Sketch of the details of the sensor window. [Pictures are taken from www.ophiropt.com.]

From time to time, we have to calibrate the pulse energies in order to check everything is functioning normally. Since our typical working energy is a few mJ's, it is very important to know how to measure this energy regime safely. The standard photodiode sensors such as the PD300 series from Ophir® are used primarily to measure the power CW lasers and have saturation threshold of only a few μJ, they cannot be used directly to measure the 10ns pulses in the mJ energy regime. A convenient and accurate method is to use a thermal sensor instead, for example, the 12A series from Ophir®. Fig. 6.3 shows an image of such a sensor, together with a sketch of the details of the sensing window. These sensors are characterised by two series of metallic junctions, the inner hotter junctions and the outer colder junctions. When a lasers pulse is impinged on the sensor disc, a temperature gradient is created between the hotter junction and the colder junction, as the radial heat flows on the disc. This temperature gradient

causes a voltage difference between the two types of junctions, which is further converted to a reading of pulse energy.

The advantages of using thermal sensors to measure pulse energy include the irrelevance of ambient temperatures and lights, and the availability of broadband sensors. Furthermore, the pulse width could be as short as possible in principle, as the whole heat transformed from the laser pulse will be integrated during the measurement. However, since it requires a few seconds for the sensing disc to heat up and cool down, we can only use these sensors for single shot measurement, where we manually trigger the laser pulses every a a few seconds.

6.2.2 Approach 1: with a Fibre

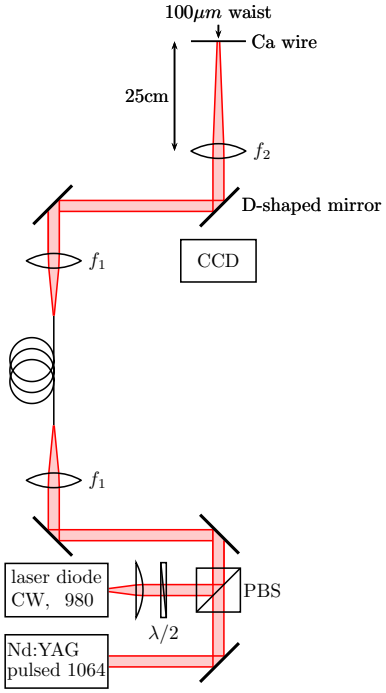

Figure 6.4: Sketch of the Fibre-Coupled Ablation Laser Feedthrough Setup. A CW laser in 980 nm and the Nd:YAG pulsed laser are co-aligned through a mirror and a PBS and both coupled to the same fibre. Then the beam out of the fibre is collimated and focused onto the Calcium granule. The final mirror in front of the cryostat's viewport is replaced by a D-shaped mirror so that the reflection can be collected in the CCD camera, with which we can precisely align the beam inside the cryostat.

In the beginning of the project, we thought it might be advantageous to couple the pulsed laser into a fibre so that the beam can be conveniently shared among distinct optical tables. Fig. 6.4 is the sketch for such a setup. Since a single pulse encompasses high intensity that could be dangerous for both the human being and the setup, we first co-aligned a Continuous-Wave (CW) laser with the pulsed laser. This CW laser is first coupled to a fibre and fed to the cryostat afterwards. Never should we turn on the pulsed laser until we have made sure CW laser was well-aligned everywhere. The wavelength for the CW laser was chosen to be $980\,\mathrm{nm}$ because of its relative vicinity to $1064\,\mathrm{nm}$ and low cost of the diode. The diode can be simply

powered by a battery and its intensity can be manipulated by rotating the waveplate placed between the diode and the Polarising Beam Splitter (PBS).

The major obstacle in front of us was to choose the optical elements correctly, due to the uniqueness of handling high-power pulsed laser. Noticing that all elements have certain damage threshold, which decreases with shorter pulses, we have to make sure that the beam power is below those thresholds at all the air-glass interfaces and the bulk of glass. Otherwise the glass could be burned, leading to the drop of power fed into the cryostat.

The chosen components for the ablation setup are listed in Tab.6.1. From this table we notice that the lowest damage threshold is limited by the broadband mirrors, $0.5\,\mathrm{J/cm^2}$. We estimate our largest radiant fluence as $H_e = 4Q_e/\pi d^2 \approx 0.07\,\mathrm{J/cm^2}$, where we have substituted $Q_e = 5\,\mathrm{mJ}$ as an upper bound of our typical working energy, and $d = 3\,\mathrm{mm}$ as the beam diameter. The fact that this estimated upper bound of fluence is well below the damage threshold guarantees all components listed in Tab.6.1 are able to function properly during our usage.

Type	Part Number	Damage Threshold ($\mathrm{J/cm^2}$)
Mirror	BB1-E03	0.5
Beam Spliter	PBS103	2
Fibre Coupling Lens	LB1471-C (f=50mm)	7.5
Focusing Lens	LB1056-C (f=250mm)	7.5
Wave Plate	WPH05M-1064	10

Table 6.1: The Chosen Optical Components, together with corresponding damage thresholds for pulsed $1064\,\mathrm{nm}$ laser. All the components listed here are from Thorlabs®.

The fibre used in setup of Fig. 6.4 is a $2\mathrm{m}$-long end-caped PCF[1]. The end-caps have a length of $1400\pm100\mu$m and diameter of of 240μm. This geometry allows the fibre to withstand an input pulse energy of $1\,\mathrm{mJ}$.

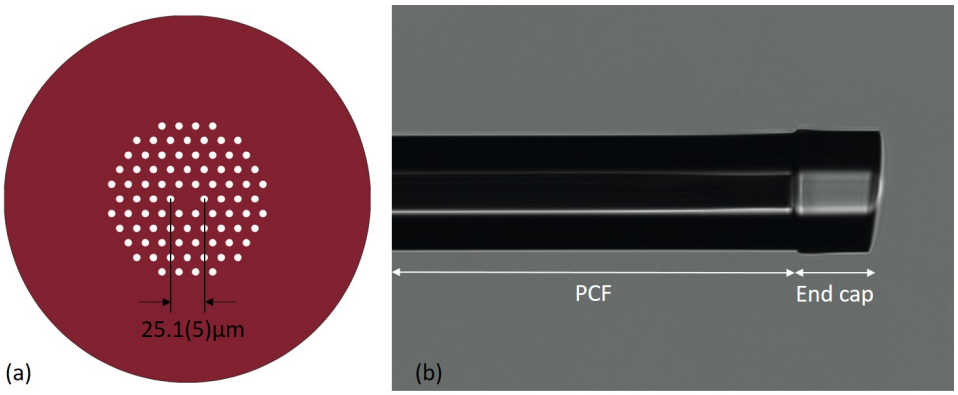

Figure 6.5: Illustration of the used fibre in our setup. (a) Interface of the PCF (LMA-25 from NKT photonics). (b) Side view of a PCF attached with an end cap (Image taken from ALPhANOV)

The coupling efficiency is measured after both the $980\,\mathrm{nm}$ and $1064\,\mathrm{nm}$ lasers are coupled

[1]Purchased from ALPhANOV. The fibre is based on LMA-25 from NKT photonics.

to the fibre. This is performed by measuring the laser powers before the fibre input connector and after the output connector. The measurement shows an efficiency of 9.1% for $980\,\mathrm{nm}$. Assuming the same coupling efficiency for the $1064\,\mathrm{nm}$ laser, the output pulse energy would be on the order of 100μJ. This amount of energy was shown to be enough for loading Calcium and Aluminium ions into the 3D trap [Guggemos15]. However, we did not manage to load ions in our cryogenic SET. Since the loading probability of our trap is generally smaller than that of a 3D trap due to its shallow trapping depth, it is suspected that pulse energy cannot create enough Calcium atoms. Therefore we decided to ramp up the pulse energy further and rebuild the setup in free space first.

6.2.3 Approach 2: without a Fibre

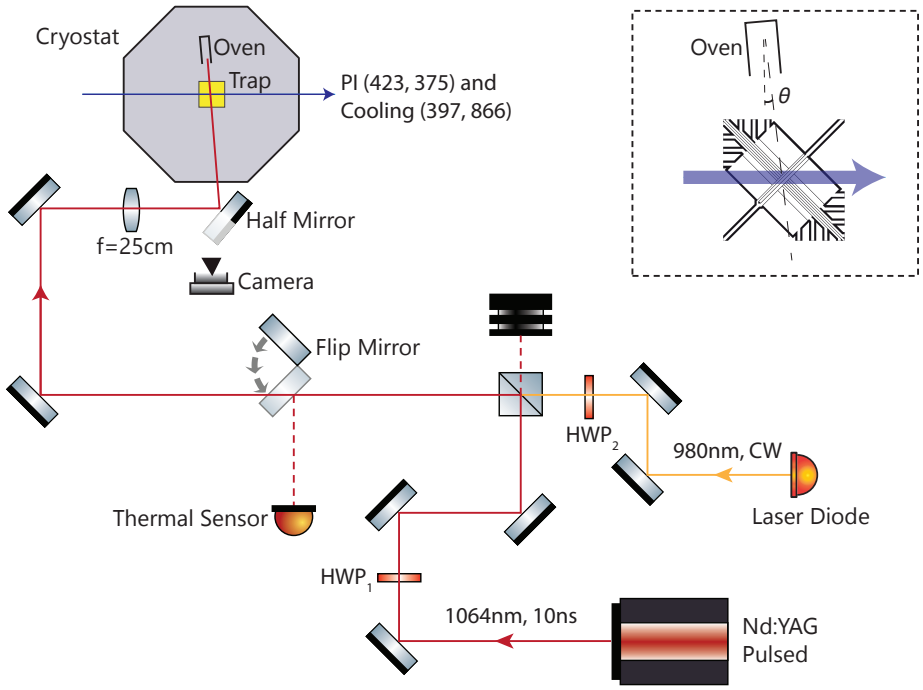

Figure 6.6: Ablation Setup in Free Space. The CW 980nm laser and the pulsed 1064nm laser are co-aligned through mirrors and a PBS. Their individual powers can be tuned by rotating the corresponding HWP's. Afterwards, the beam is directed to the cryostat without usage of a fibre. A flip mirror is mounted in the middle in order to calibrate the energy of the pulsed laser when necessary, using a thermal sensor. The precise focusing position of the beam in the oven can be walked by tweaking the half mirror in front of the cryostat viewport. Behind the half mirror there is a camera in order to capture the reflection of the lasers from the oven. The insert show the relative orientation of the oven, trapping axis and laser beams (not to scale). The opening of the oven tube forms a small angle of θ with the normal of the laser direction.

Now that we have noticed that the power of the pulsed laser out of a fibre was never high enough, we decided to remove the fibre for the moment and rebuilt the setup in free space. After all, the original motivation to incorporate a fibre was out of convenience.

After removing the fibre, we have to place the beam path of the pulsed laser at the same level

as the cryostat's viewport. Fig. 6.6 shows the sketch of the final setup. Without the guidance and shielding from a fibre, it is extremely important to make sure the whole setup is well shielded.

With careful alignment, we managed to observe the focused spot of the pulsed laser inside the oven, as in Fig. 6.7, together with a comparison when no lasers are on the oven. To obtain this photo, we first take the photo with only CW 980 laser in order to make sure the focused spot lying inside the oven tube. Then we block the CW laser and start to manually trigger the pulsed laser while taking a series of photos automatically with the camera. The control software of the camera allows us to take 10 photos per seconds, and in most cases we are able to capture the pulse from a single trigger.

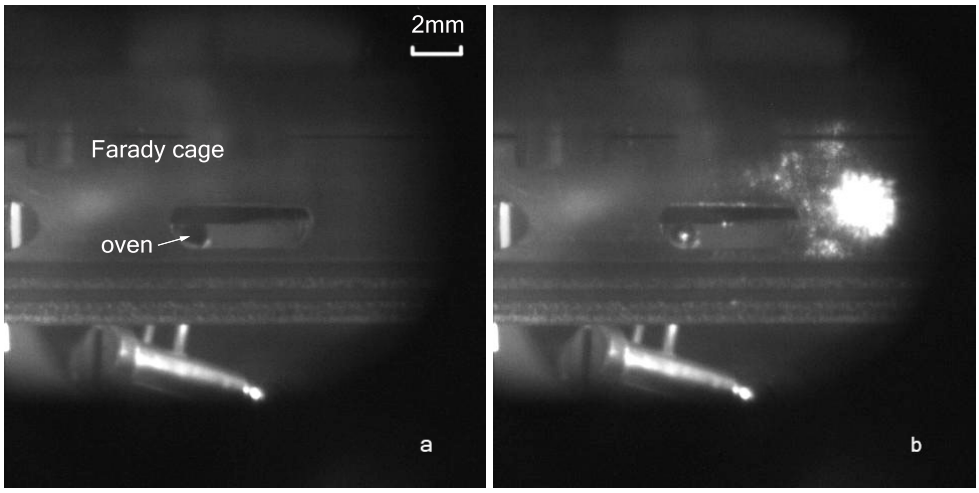

Figure 6.7: Photos of the oven when (**a**) all lasers are off and (**b**) the pulsed 1064nm laser is well aligned and focused. The bright area in the right side of (**b**) is due to the reflection from the glass window between the Farady cage and the viewport.

From Fig. 6.7, we can conclude that the pulsed laser is well focused into the oven. Due to multiple filters applied in order to take the photos, however, it is most likely to say that the actual size of the focused spot is larger than the observed bright spot in the photo. With rough estimation, the MFD of the focused spot should be around 100μm to 200μm.

In order to quantitatively recognise how much energy is illuminated to the Calcium granule in each experiment, we performed a calibration of the laser pulse energy by rotating the HWP_1 in Fig. 6.6 and measuring the pulse energy with the thermal sensor. The result is shown in Fig. 6.8.

When the new setup was finished, we successfully obtained positive signals without much efforts. Fig. 6.9 shows a detailed process of loading two ions with ablation. Before this, we have engineered the electrode voltages such that we can load successfully with effusive oven, and the ion remains stable in the trapping potential.

We managed to load one ion with 5 pulses and load another one with 30 pulses. These are one order of magnitude shorter than the typical loading times using effusive oven. Furthermore, we notice that the one ion can stay stable once loaded, whereas two ions becomes unstable immediately under interruption of a single ablation pulse.

Apart from the lucky scenarios in Fig. 6.9 where we can load ions within a few pulses,

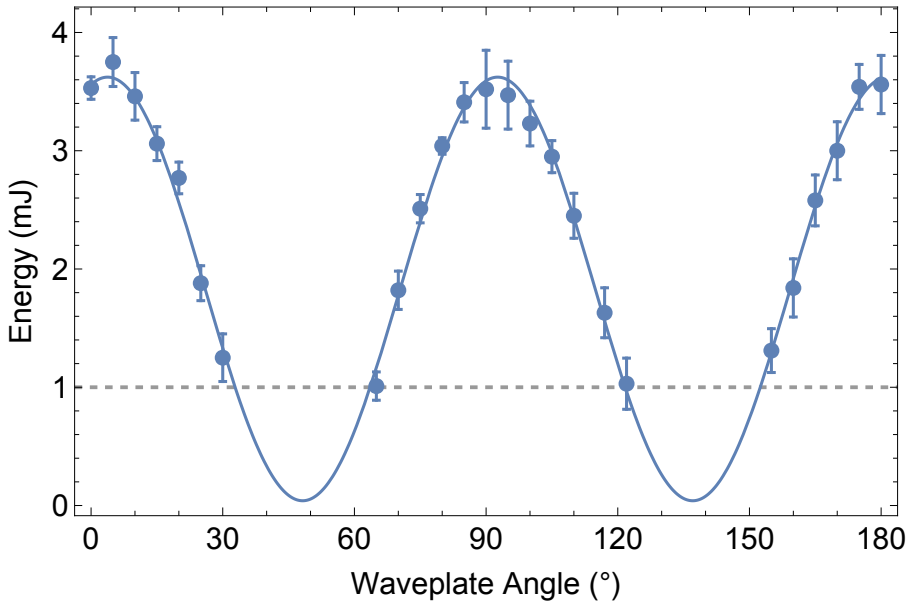

Figure 6.8: Calibration of Pulsed Laser Energy. The horizontal axis denotes the angle of HWP_1 and the data points are measured energy using the thermal sensor, for each angles. The blue line is a fitting with Cosine. And the dashed line indicates the sensitivity threshold of the sensor.

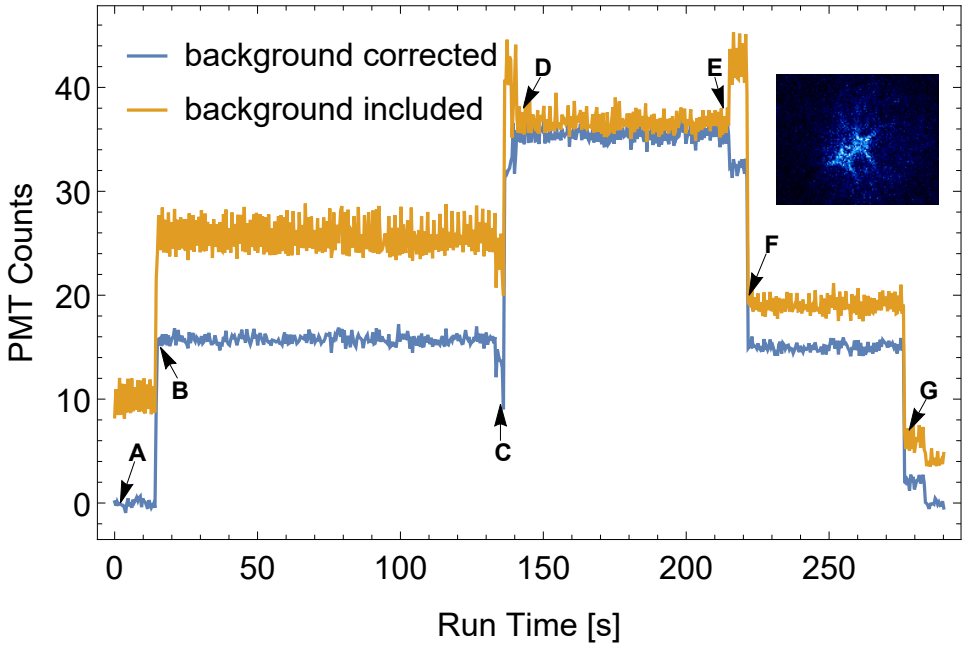

Figure 6.9: A running-time plot of PMT counts for two ablation-loaded ions. The blue and yellow lines denote the counts with and without background correction in the CoolDet sequence, respectively. The marked time points represent: (**A**) manually trigger ablation laser every 2 or 3 seconds; (**B**) load first ion after 5 pulses; (**C**) load second ion after about 30 manual triggers; (**D**) block 397 ^{0}th beam to check the stability of two ions; (**E**) unblock 397 ^{0}th; (**F**) put half count into A CMOS camera and the image of two ions is shown as insert; (**G**) try to load a third ion, but one ion get lost immediately after a single pulse, and a few seconds later the other ion get lost as well. Both PI lasers are turned on throughout the experiment.

in most cases, however, we did not manage to load ions with ablation. Nevertheless, we still observe correlated signals as we trigger laser pulses. Fig. 6.10 shows a process where we illuminate laser pulses to the oven while one ion has been loaded with effusive oven. In this case, no further ions are loaded, but the loaded ion are kicked out under the effect of laser pulses. This signal indicates that we have created an atom plume with the pulsed laser, and as the atoms flying across the trapping region, the loaded ion interacts with them and eventually gain enough kinetic energy to overpass the trapping barrier.

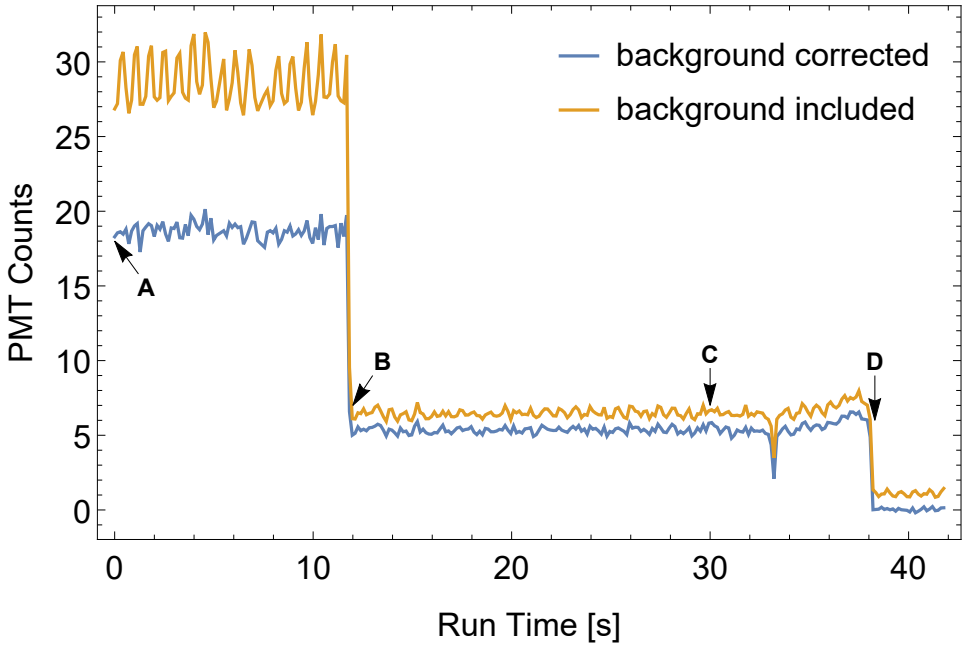

Figure 6.10: A running-time plot of PMT counts for a kicked-out ion with ablation laser. The blue and yellow lines denote the counts with and without background correction in the CoolDet sequence, respectively. And the marked time points represent: (**A**) One ion loaded with effusive oven and stayed in an non-optimised potential; (**B**) Turn off 397 ^{0}th to check the stability of the ion; (**C**) turn on PI lasers and start the pulsed laser in 3Hz continuous mode; (**D**) Observation of the ion getting kicked out.

6.3 Quantitative Analysis on Neutral Atom Ablation Plume

Generally speaking, loading an ion is a low probability event, due to the fact that only one or two ions are successfully captured by the trapping potential from a whole cloud of neutral atoms. In addition, the loaded ions can be affected by the residue ions and atoms from the plume. Once in a while we have to re-calibrate the electrode voltages in order to identify a favourable loading potential.

Compared to ion loading, creating a plume of neutral atoms requires less efforts and simpler setup. We mainly need to deal with the laser setup without concerning too much on the trap electrodes. Meanwhile, this process is remarkably reproducible, because all the laser parameters could be well calibrated and maintained stable. Taking all these facts into account, we expect it would be useful to analyse the ablation plume systematically. In the following of this section, the experimental setup for analysing the neutral atom plum is introduced, together with the results of velocity distribution and its dependence on the pulse energies. These studies constitute the groundwork for the next-generation design of the ion loading architectures.

6.3.1 Experimental Setup

Before the start of a particular experiment, it is necessary to check everything is well functioning. In our case, we could first load an ion with effusive oven. Afterwards we manually trigger a few 1064 pulses with energies around 2.5mJ. If the loaded ion can be knocked out under these pulses, it confirms that the laser pulses has successfully created neutral atom plume and the Calcium granule is not locally depleted.

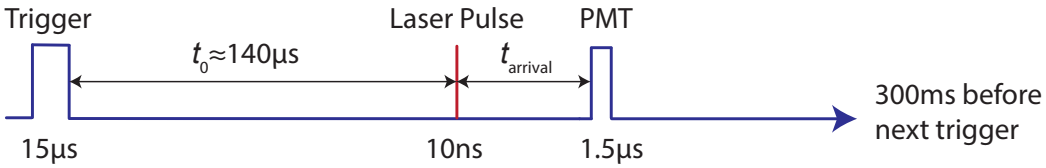

Figure 6.11: Sequence For Analysing Ablated Neutral Atom Plume. A standard trigger pulse is sent from the DDS board to the flashlamp in the laser head, through the TTL trigger pulse. After a latency of around 140ns, the laser pulse will be illuminated. Later on, the PMT window is open for $1.5\mu s$ after certain time, which captures the atoms in a certain velocity range. The sequence is repeated every 300ms, due to the low limit of the laser's repetition rate.

In order to control the pulsed laser remotely and acquire data automatically, we designed a new sequence in Xilinx (Fig. 6.11)) and wrote an independent experimental frame in Ionizer. In the rear of the laser's power supply, we set the flashlamp source to be external and the Q-switch source to be internal. The TRIG IN port of the flashlamp source is connected to a TTL channel through a 5m-long BNC cable. With this setup, the pulsed laser could be externally triggered by a high voltage ($> 3.3\,\mathrm{V}$) pulse through the TTL interface. After one triggering pulse, it takes a latency of around 140μs for a laser pulse to be generated. Apart from the pulsed laser, only the 423nm laser is fed to the cryostat in order to drive the transition ${}^1S_0 \leftrightarrow {}^1P_1$ of ^{40}Ca atom. The

laser pulse is sent to the oven through the optical setup described in the last section, and we wait for a scannable time until we open the PMT channel for 1.5μs to read the photon counts. The PMT collects the fluorescence from the ${}^1S_0 \leftrightarrow {}^1P_1$ transition and the readings are a quantitative measure of the velocity-resolved neutral atom numbers. We choose the PMT time window to be as short as 1.5μs because our typical resolution for scanning the arrival time is 2μs to 5μs. This choice allows the data points at different arrival times to be mutually independent.

6.3.2 TOF Spectrum and Velocity Distribution

In this experiment, we fix the HWP for the pulsed laser at $20°$, hence the laser pulses have energies of around 2.5mJ. The frequency of the 423nm laser is tuned by manually rotating the controlling knob for the grating of the 846 laser. This gives us a tuning range of around 1.5GHz with resolution of 200MHz. Fig. 6.12 shows a Time-of-Flight (TOF) spectrum of the neutral atoms, with respect to the frequency of the 423 laser.

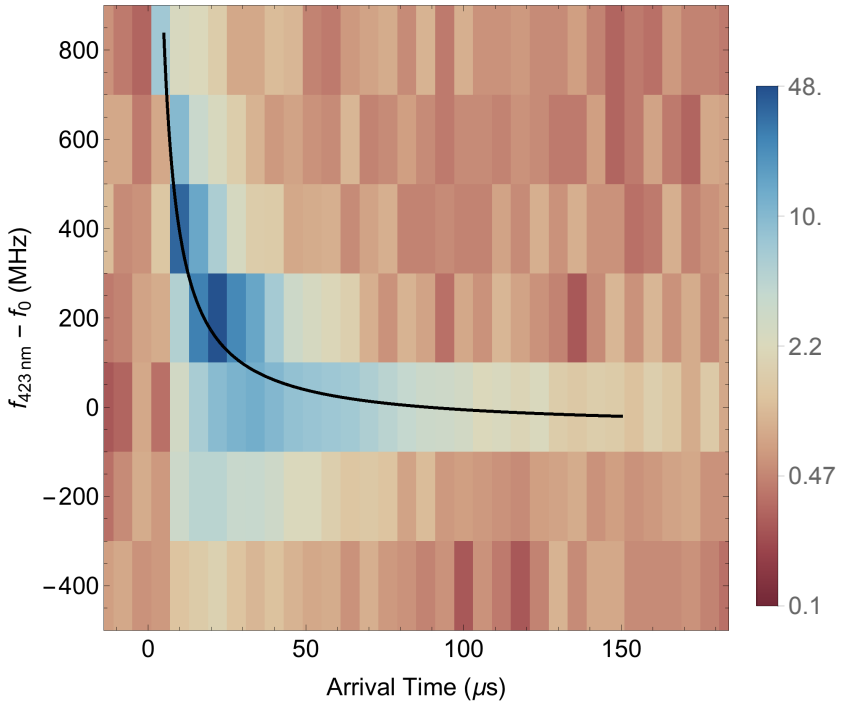

Figure 6.12: Time-of-Flight Spectroscopy of neutral ^{40}Ca atom fluorescence. The horizontal axis denotes the travelling time of the atoms from being ablated to being captured by the 423nm laser. And the vertical axis specifies the detuning of the 423nm laser, relative to the typical frequency for loading with effusive oven, $f_0 = 709.0784(1)$ THz. The plot is shown in logarithmic scale. The black curve represents the theoretical Doppler-shifted resonance, for an angle between the atom plume and the laser of $4.3°$.

In Fig. 6.12, we compare the PI frequency with respect to the typical frequency used for loading with effusive oven, $f_0 = 709.0784(1)$THz. We can observe that the maximum peak happens at f_0+200MHz, whereas the broadest peak is located at f_0. Furthermore, as we increase the PI frequency, we notice that the peak is shift leftwards. This coincides with the Doppler effect. In our setup, the direction of the oven tube forms an angle smaller than $90°$ relative to

the beam path of the PI laser. The finite velocity component projected in the direction of the beam path gives rise to a red-shifted laser frequency, and this effect increases with the atom velocity. Therefore a bluer PI laser would be resonant to with the faster atoms. To analyse the contribution of Doppler shift, I fit the peak position for different PI frequency to the equation:

$$\frac{f_{\text{obs}}}{f_{\text{lab}}} = 1 - \frac{d \sin\theta}{c t_{\text{peak}}}, \tag{6.1}$$

where f_{obs} is the laser frequency observed by the atom, f_{lab} is the laser frequency in lab frame, d the distance between the oven and the trap, t_{peak} the peak arrival time for each laser frequency, c the speed of light in vacuum, and θ the angle between the oven direction and the normal of the PI laser beam path. By setting $d = 25$mm, we can roughly estimate θ to be around 4.3°.

The observation that the peak is the broadest at f_0 also explains why we only managed to load the ion with this 423 frequency in our ablation trials, At this frequency, the laser captures the slower atoms that have lower kinetic energy than the trapping depth.

In order to obtain the frequency-independent velocity distribution of the ablation plume, we sum up the photon counts along each vertical line in Fig. 6.12, and convert the horizontal axis to velocity simply by $v = d/t$ where $d = 25$mm. Due to the fact that the transition ${}^1S_0 \leftrightarrow {}^1P_1$ is a closed transition, the PMT counts are considered inversely propotional to the atom velocity [Guggemos15]. Therefore we need to re-scale the PMT counts by multiplying their corresponding atom velocities to account for this effect. The final result is shown in Fig. 6.13. We fit this with the Maxwell-Boltzmann Speed Distribution:

$$A \cdot f_{\text{MB}}(v;T) = A \left(\frac{m}{2\pi k T}\right)^{3/2} 4\pi v^2 e^{-\frac{mv^2}{2kT}}, \tag{6.2}$$

where A is the scaling factor, T the temperature in Kelvin, m the atomic mass, k the Boltzmann constant and obtain $T = 7937(408)$K, which is one order of magnitude larger than the typical temperature of effusive oven. This number, as a matter of fact, is not absolutely illustrative, due to the fact that the ablation scheme is not a thermalised process and hence hence there is no well defined temperature.

To better understand the ablation scheme, we further fed both PI lasers (423nm and 375nm) to the cryostat and performed the same experiment. The results show no apparent differences. This confirms that in the pulse energy region of our consideration, the majority of the ablation plume is indeed the neutral atoms in the electronically ground state.

6.3.3 Pulse Energy Dependence

In the above experiment, we have set the pulsed laser at a fixed energy. Apparently, pulse energy is a crucial parameter for ablation loading. If the pulse energy is too low, we cannot overcome the surface bounding energy to create sufficient free atoms. On the other hand, shining a high pulse to the Calcium granule might create atom plume beyond necessary, notwithstanding the danger of misalignment. The increased collision rate among them may raise the difficulty of ion loading. Furthermore, if we shoot high-energy laser pulses repeatably to a fixed position at

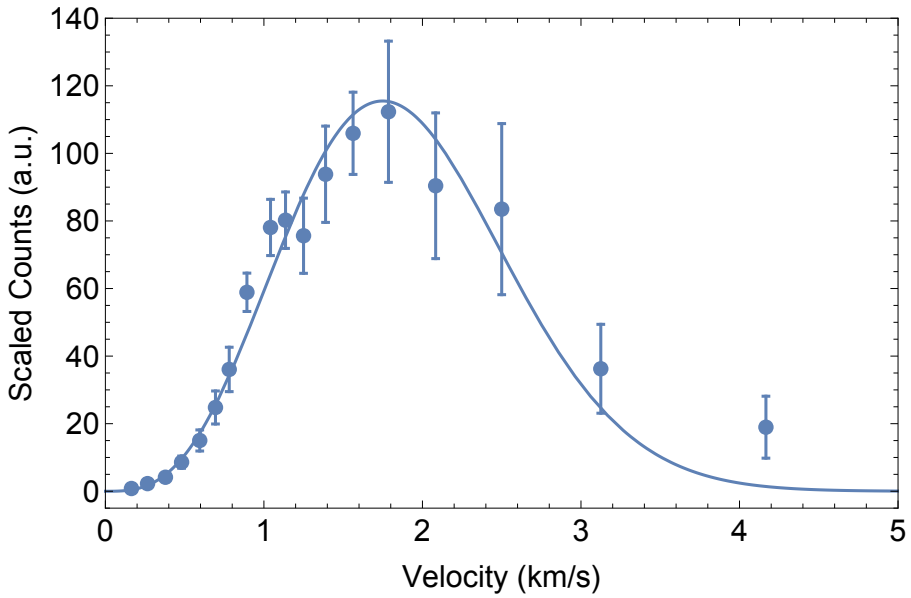

Figure 6.13: Velocity Distribution and Fitting with Maxwell Distribution. The vertical axis denotes the frequency-summed-up PMT counts in Fig. 6.12, times the corresponding atom velocities.

the granule, we might locally deplete the sample and have to move the spot. In order to identify the best pulse energy for ablation loading, we now perform the similar experiments for various pulse energies and analyse its influence on the velocity distribution of neutral atoms.

To tune the pulse energy, we rotate the HWP_1 in Fig. 6.6 to different angles, and refer to Fig. 6.8 for corresponding energies. Following the analysis process above, the measurement results and fitted velocity distributions are shown in Fig. 6.14. From this plot we notice that as we decrease the pulse energy, the peak velocity has gradually shifted leftwards, and the peak height decreases. These indicate that lower energy pulses produce fewer and overall slower atoms.

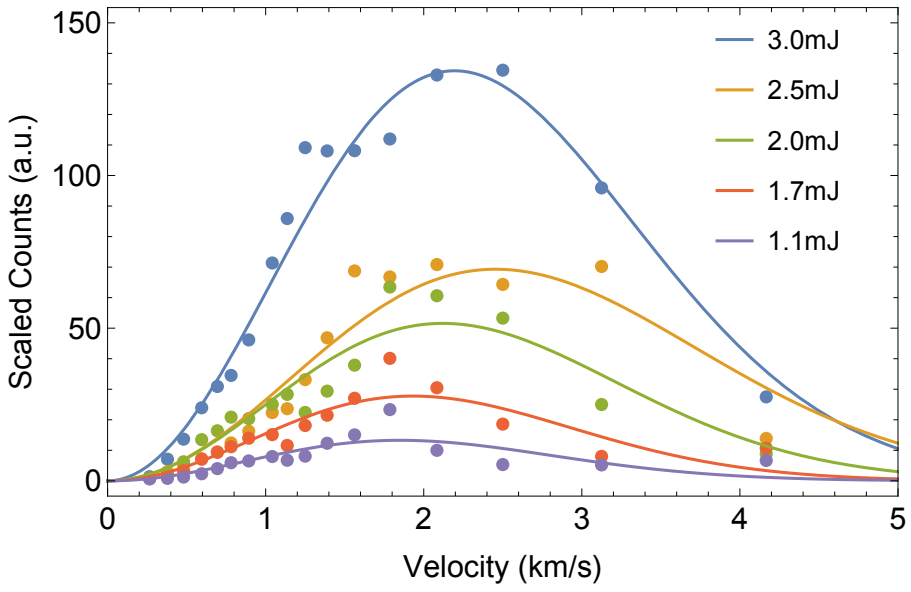

Figure 6.14: Velocity Distribution for different pulse energies, together with fittings with Maxwell Distribution.

Since the values of the fitted temperatures do not have clear physical meanings, we continue the data analysis to estimate the fraction of atoms in the low velocity range for each pulse energy. After all, it is this low-velocity tail that determines the loading probability. We convert the trapping depth to thermal velocity through the equipartition theorem in one dimension:

$$v_{\text{th}} = \sqrt{\frac{k_B T_{\text{depth}}}{m}} \approx 1.44\,\text{km/s}, \tag{6.3}$$

where k_B is the Boltzmann constant, m is the mass of Calcium ion, and we have inserted $T_{\text{depth}} = 10\,\text{mK}$ as our estimated trapping depth.

Based on this, we calculate the fraction of low-velocity tail for each fitted curve in Fig. 6.14 as

$$frac(T) = \frac{F_1(T)}{F_2(T)} = \frac{\int_0^{v_{\text{th}}} f_{\text{MB}}(v,T)\,\mathrm{d}v}{\int_0^{\infty} f_{\text{MB}}(v,T)\,\mathrm{d}v}, \tag{6.4}$$

and the final results are shown in Fig. 6.15. Noticing the uncertainty of fitting, we also estimated the standard errors of $frac(T)$ using the law of error propagation:

$$\begin{aligned} \sigma_{frac} &\approx frac \cdot \sqrt{\left(\frac{\sigma_{F_1}}{F_2}\right)^2 + \left(\frac{\sigma_{F_2}}{F_1}\right)^2 - 2\frac{\sigma_{F_1F_2}}{F_1F_2}} \\ &\lesssim frac \cdot \sqrt{\left(\frac{\sigma_{F_1}}{F_2}\right)^2 + \left(\frac{\sigma_{F_2}}{F_1}\right)^2}, \end{aligned} \tag{6.5}$$

where σ_{F_1} and σ_{F_2} are standard errors of $F_1(T)$ and $F_2(T)$, respectively, and $\sigma_{F_1F_2}$ is the covariance between them. We have neglected the covariance term in the second line of the equation to simplify our calculation, and the two standard errors are given by

$$\begin{aligned} \sigma_{F_1(T)} &= \int_0^{v_{\text{th}}} \frac{\partial f_{\text{MB}}}{\partial T}\,\mathrm{d}v\,\sigma_T, \\ \sigma_{F_2(T)} &= \int_0^{\infty} \frac{\partial f_{\text{MB}}}{\partial T}\,\mathrm{d}v\,\sigma_T, \end{aligned} \tag{6.6}$$

where σ_T is the standard error of fitted temperature, for each curve in Fig. 6.14.

Despite of the relative large error bars in Fig. 6.15, we can qualitatively argue that when the pulse energy is below around $2.5\,\text{mJ}$, the fraction of low-velocity tail increases as we decrease the pulse energy. As a result, the theoretical probability of ion loading increases with decreasing pulse energy. However, if the pulse energy is too low, the total atoms that are ablated from the pulse gets too few, hence decreasing the probability of ion loading. Take both arguments into consideration, we would expect the ideal pulse energy falls in the regime $1.5\,\text{mJ}$ to $2.0\,\text{mJ}$.

6.4 Conclusions

In this chapter an optical setup is built to upgrade the ion-loading scheme from the effusive oven method to an all-optical method, namely ablation loading. The ablation loading scheme offers multiple advantages over the effusive oven scheme, including shorter loading time, no heating of the UHV chamber, and better possibility of loading more ions. A setup that includes

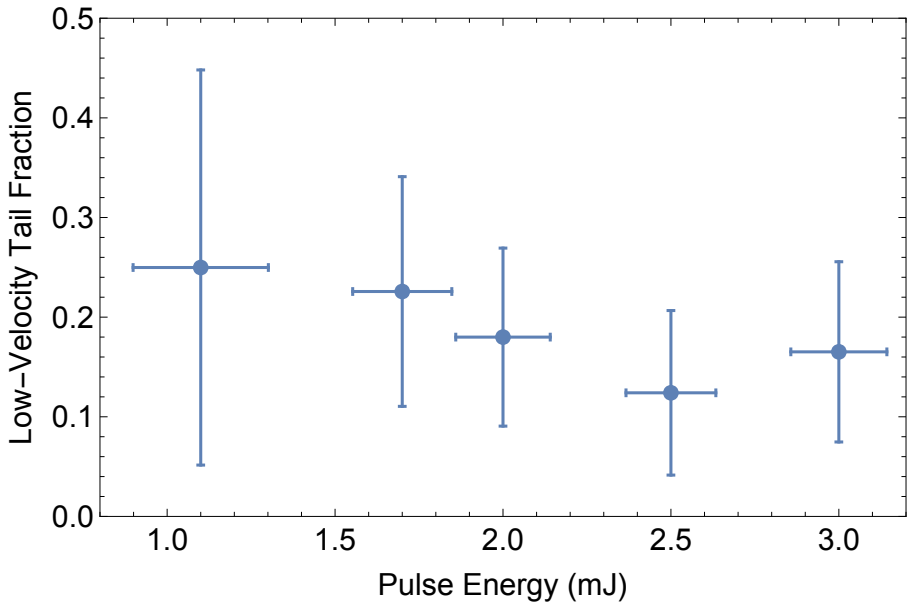

Figure 6.15: Fraction of atom numbers in the low-velocity tail, as a function of pulse energies. Each data point corresponds to a fitted line in Fig. 6.14, together with propagated standard error (see text for analysis).

a high-power fibre was firstly examined, but later it shows that the output energy were not high enough to create enough ablation plume. Therefore the setup was rebuilt such that the ablation laser was propagating through free space.

Successful multiple ion loading were demonstrated by this free-space setup. In order to find the best loading parameters, we performed a quantitative analysis on the neutral atom plume. This includes measuring the Time-of-Flight Spectrum and obtaining the velocity distribution for different pulse energies. An analysis on the low-velocity atom number fraction shows that a pulse energy between $1.5\,\mathrm{mJ}$ and $2.0\,\mathrm{mJ}$ would be optimal.

Due to the geometrical limit of our setup, the distance between the final focusing lens and the oven tube has to be as far as $25\,\mathrm{mm}$. This raises the difficulty of studying the effect of different ablation angle. By bringing the oven tube closer to the focusing lens, it is suspected that the optimal energy can be lower.

CHAPTER 7

Summary and Outlook

7.1 Summary

This thesis is focused on motional state engineering and a setup for an all-optical ion loading scheme.

In the motional state engineering, we performed fast switching experiments and micromotion experiments. The reason for the long-standing issue in the voltage change on the filter capacitors during the switching cycle were found to be the finite propagation times of the switches. In previous experiment, this overlooked property leads to a direct shorting between the filter capacitors for a time of $30\,\mathrm{ns}$. By introducing a delay time in the Break-Before-Make experiments, we observe a mitigation of the voltage change. Furthermore, we designed an off-time switching experiment to calibrate the propagation time for each switch and found out the underling reason of losing ion when $t_{\mathrm{delay}} > 30\,\mathrm{ns}$. These experiments put new insights into the creation of a squeezed vacuum state through fast switching.

This thesis laid down foundational works in micromotion engineering, which opens a new scheme for single ion addressing. This is realised by adding a perturbation Hessian matrix with non-zero off-diagonal elements to the Hessian matrix of a micromotion compensated trapping potential. The ions sitting at different positions along the trapping axis hence experience different excess micromotion modulation, which leads to a discrepancy in the carrier Rabi frequencies. Preliminary experimental results were shown for two-ion experiments. By choosing the global driving time correctly for the carrier transition, we can flip the state of one ion while keeping the other unchanged.

Due to the drawbacks of the current ion loading method with effusive oven, an all-optical ion loading setup were built. This involves a usage of a pulsed laser with a few mJ. Successful scenarios for loading multiple ions in this new scheme have been found, followed by a systematic study on the ablated neutral atom plume.

7.2 Future Work

This thesis provides insights to future works in different aspects:

- The fast switching experiment is a follow-up study to the prior experiments on large coherent state creation [Alonso16]. After finding and calibrating the previously overlook

property of propagation delay times, it provides an important factor in the future designing of bang-bang control sequences. Furthermore, it offers a new guidance to the wiring of the switches. In our experiment, the three switches of an IC are connected to form a 3:1 multiplexer. Due to the nature of the propagation times, we have to perform BBM switching to reduce the overlap between different switches. A better circuitry might be controlling the switches individually such that the propagation times do not need to be considered.

- The micromotion engineering experiment is the ground work for a new single ion addressing scheme. With better two-ion loading method and more calibration of the tilting effect of the trapping axis, these work would be proved more useful. This scheme can become a more versatile toolbox for single-ion rotation and single-ion addressing if the 729 nm and the 397 nm lasers can be tuned to the micromotion sideband. In our current experimental setup, this is hard to achieve since the RF frequency is beyond the bandwidth of the AOMs used. Working with lower RF frequency or replacing the AOMs could make it easier to tune the lasers to the micromotion sideband.
- In the ablation loading experiment, an all-optical ion loading method has been built up and successful loading scenarios have been realised. These efforts will be useful for future designing of the cryogenic surface-electrode trap experiments. By a better organisation of the laser beam and oven geometry, a higher loading probability and better repetitiveness are feasible.

APPENDIX A

Temperature Cycling for Large Capacitors

When finding the explanation for our observations in the previous fast switching experiments as shown in Fig. 4.5, we first thought the capacitance of the filter capacitors were too low. These capacitors were formed by two in-parallel capacitors with capacitance of $100\mathrm{nF}$ and $3\mathrm{nF}$, giving rist to a total capacitance of $103\,\mathrm{nF}$ (Fig. 3.2). In the very beginning, we thought that the effect of voltage change can be mitigated if these capacitors were replaced by the ones with larger capacitance. Since these capacitors have to work under $4\mathrm{K}$, it is important to make sure where they are performed normally at this condition. To do this, we ran a few temperature cycles for these capacitors. Even though these experiments were unused in this thesis, it might be relevant for potential readers.

Label	Designed Capacitance (μF)	Size (mm)	Quantity	Manufacturer Part Number
10a	$10 \pm 20\%$	57×50	3	25ST106MD15750
22a	$22 \pm 20\%$	57×50	3	16ST226MD35750
22b	$22 \pm 20\%$	57×50	4	16MU226MD35750

Table A.1: Details of tested capacitors. All the capacitors are manufactured by Rubycon®. The designed capacitance is shown for working condition at -55°C ~125°C.

We tested 10 capacitors of three different types in total, with capacitance two order of magnitude larger than the current used ones. The experiments were performed in a cryostat in the Optical Trapping team at TIQI. Fig. A.1 shows the images of the setup. The tested capacitors are soldered onto a homemade PCB, which mechanically and thermally connected the Copper platform of the cryogenic chamber. The electric connection is enabled by the wiring from the PCB to the feedthrough of the chamber. The cryostat is able to run a full temperature cycle between room temperature to 4K in about 8 hours. Outside the cryostat, we measure the capacitance with a normal multimeter.

12 temperatures cycles are performed in 6 days, and the measurement results of the capacitance are shown in Fig. A.2. From Fig. A.2a we notice that there is a direct correlation between the capacitance and temperature. As temperature decreases, the capacitance also decreases. Furthermore, all capacitors remain functioning for the temperature down to $4\,\mathrm{K}$, which

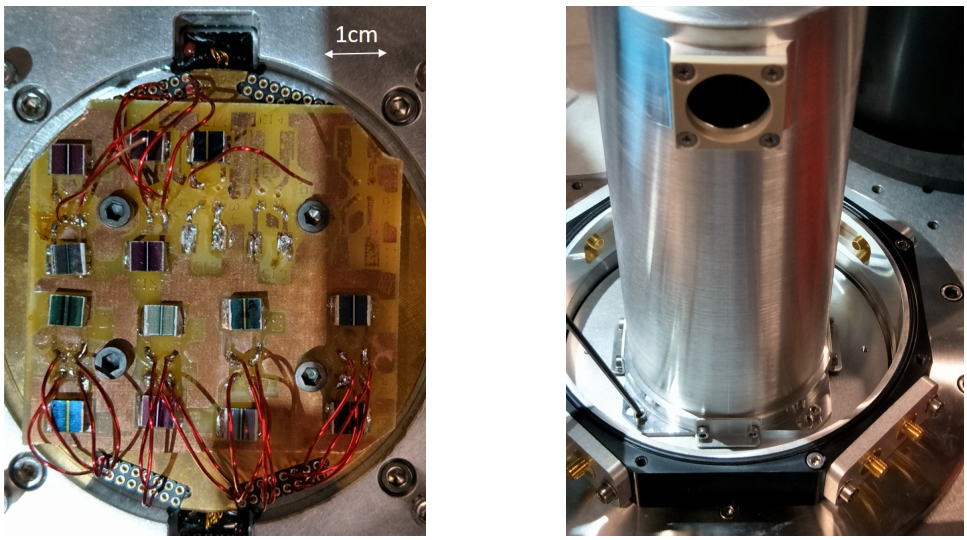

(a) (b)

Figure A.1: Experimental setup for temperature cycling. (a) Image of the tested capacitors, mounting PCF and wiring to the electric feedthrough of the cryostat. 13 capacitors are soldered to the PCB, but only 10 of them are electrically connected to the feedthrought, as listed in Tab. A.1. (b) Image of the Outside of the vacuum chamber.

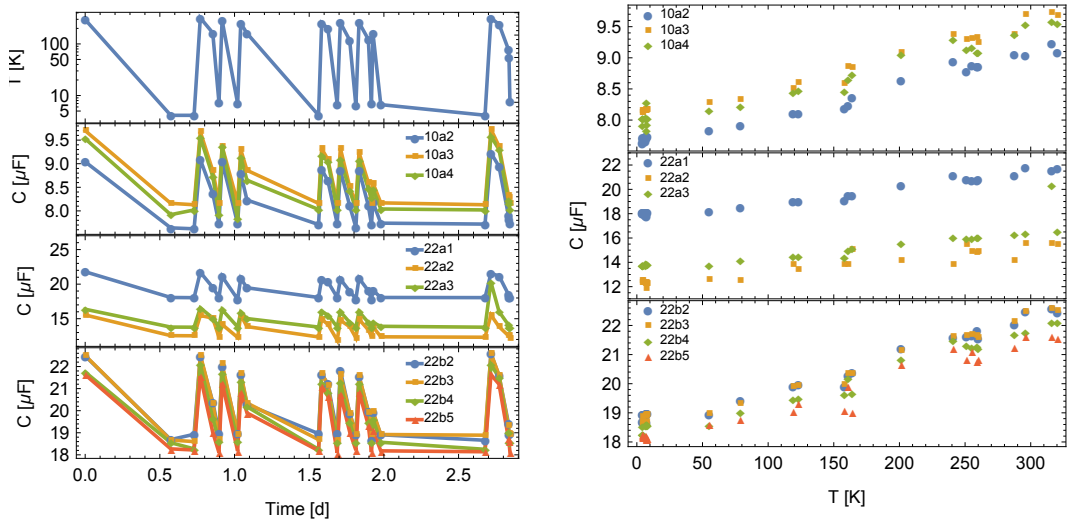

(a) (b)

Figure A.2: Measurement Results of Temperature Cycling. (a) Run-time results. The top panel is the recording of the temperature of the chamber, and the lower three panels are measurements for three different capacitors in Tab. A.1 (b) Capacitance versurs Temperature for three types of capacitors.

are well below the characterised condition from the manufacture. However, the capacitors with label 22b have more stable performance than 22a. In Fig. A.2b the capacitance are plotted as a function of temperature. We further notice that their correlation is roughly linear.

As a summary, the capacitors with capacitance at 10 μF order of magnitude are still working at 4K, with a drop of capacitance of around 20%.

APPENDIX B

Data Analysis of Fast Switching Experiments

In chapter 4 when analysing the experimental results in Fig. 4.10 and Fig. 4.13, it is important to find correct displacement size $|\alpha|$ for $t_{\text{off}} > 30\,\text{ns}$. Due to the complex function form of the fitting function Eq. (4.10),

$$P_S(t_p;\alpha) = \frac{1}{2}\sum_{n\geq 0} p_{n_{\text{th}},\alpha}(n)\Big[1 + e^{-\gamma t_p}\cos(\Omega_{n,n+1}t_p)\Big], \tag{B.1}$$

a direct NonLinearModelFit in Mathematica® is unavailable. In this appendix, the basis of the algorithm to numerically find $|\alpha|$ is described.

In Eq. (B.1), all the parameters except α is treated as known. The fitting problem is therefore in fact a one-dimensional problem. We therefore construct an objective function using the least-squares method:

$$\begin{aligned} S(\alpha) &= \sum_{t_p} w_{t_p} r^2_{t_p,\alpha} \\ &= \sum_{t_p} w_{t_p}[p(t_p) - P_S(t_p;\alpha)]^2, \end{aligned} \tag{B.2}$$

where $r_{t_p,\alpha}$ is the residual for the measurement at t_p with fitting value being α, $P_S(t_p;\alpha)$ is the predicted value and $p(t_p)$ is the actual value. The pre-factor w_{t_p} is the weighting function to take into account the quantum projection noise [Itano93] with form

$$w_{t_p}(p,N) = \frac{N}{p(1-p)}, \tag{B.3}$$

where N is the number of measurement for each t_p and p is the measured $|S\rangle$ state population. This specific form is due to the fact that the repetitive measurement of the qubit state follows a binominal distribution $B(n,p)$, and the weighting function is assigned as the inverse of the relative variance [Bevington03]. A larger weight is assigned for measurement result close to 0 and 1, and a smaller weight for results close to 0.5. This is consistence with the decoherence of the qubit state. In Fig. B.1 the weighting functions for different N are plotted. In our experiment, we take $N = 50$.

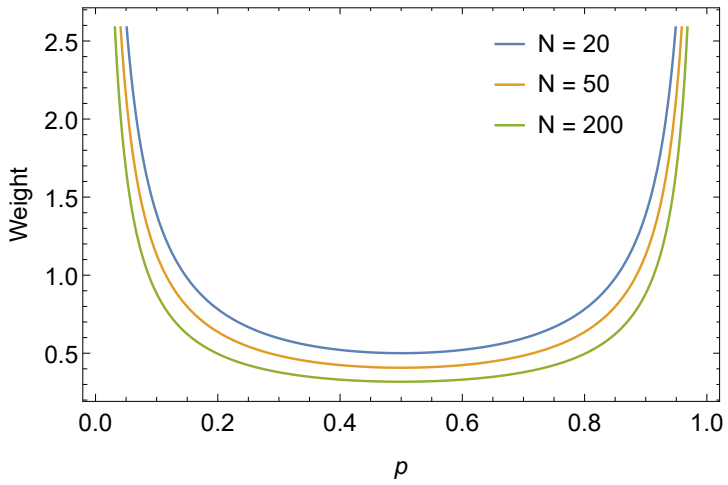

Figure B.1: Weighting function according to Eq. (B.3). The three lines corresponds to different number of repetitive measurement.

In order to minimise the objective function Eq. (B.2) and find the best fitting parameter α, it is necessary to set the initial guess and parameter range. This is realised by fitting the function with a random guess and a relatively large parameter range in the beginning, followed by a manual adaption according to Eq. (4.6).

To minimise $S(\alpha)$, we first perform an interpolation of the discrete function to obtain a continuous function $S_c(\alpha)$. Afterwards we use the built-in NMinimize function to minimise $S(\alpha)$ with respect to α. Overall, if the fitted value is α^*, the uncertainty is $\sqrt{2/S_c''(\alpha^*)}$, which is the square root of the inverse to the pre-factor of the second term in Taylor expansion of $S_c(\alpha)$ at α^*.

APPENDIX C

Python Snippets of Micromotion Engineering

In chapter 5 the micromotion-enabled single ion addressing scheme was examined. To do this we need to engineer a DC voltage set that tilts the trapping potential around the pseudo-potential minimum such that ions sitting at different positions along the trapping axis experience different modulation of excess micromotion. This is realised through a two-step minimising problem. First, a micromotion compensated trapping potential is engineered through the existing python module. The calculated voltages for the 19 electrodes of the trap are denoted as V_0 in the following. Second, a "perturbation voltage set" V_1 is added to V_0 for each electrode according to the off diagonal elements Hess_{yx} and $\text{Hess}_{z}x$ in the Hessian matrix. The numerical condition in the minimising problem is given by:

```
#import numpy as np
cons_Field = {'type': 'eq',
              'fun': lambda volts: np.tensordot(volts, GradDC, (0, 0))}
cons_Hess_x = {'type': 'eq',
               'fun': lambda volts: (np.tensordot(volts, HessDC[:,0], (0, 0))
                                     - np.array([0., Hess_YX, Hess_ZX]))}
cons = (cons_Field, cons_Hessian_x)
```

Listing C.1: Condition for the Minimising Problem

Here *GradDC* and *HessDC* are pre-calculated electric field and Hessian matrix for each electrode with $1\,\mathrm{V}$ voltage, using the *SurfacePattern* package [Schmied09; Schmied]. Due to the fact that the Hessian matrix is symmetric, only its first row needs to be constrained.

$V1$ is obtained by minimising the ℓ_2 norm of the vector of all voltages:

```
#from numpy import linalg as LA
fun = lambda volts: LA.norm(volts)
res = minimize(fun, voltages, method='SLSQP', bounds=bnds,  constraints=cons)
```

Listing C.2: Objective Function and Minimising Method

APPENDIX D

Gaussian Beams for Ablation Laser Setup

This appendix lists some of the most important formulas for Gaussian beams. More general and complete mathematics can be referred from [Siegman86].

D.1 Free Space Propagation

For a Gaussian beam propagating in the $+z$ direction and having a circular profile in the x, y-plane, the relative electric field and magnetic field strength can be expressed as, in the cylindrical coordinate,

$$u(r,z) = \frac{1}{q(z)} \exp\left\{-ik\frac{r^2}{2q(z)}\right\}, \tag{D.1}$$

where $k = 2\pi/\lambda$ is the wave number for a wavelength λ and $q(z)$ is the complex beam parameter given by

$$\frac{1}{q(z)} = \frac{1}{R(z)} - i\frac{\lambda}{\pi\omega^2(z)}, \tag{D.2}$$

with $R(z)$ being the radius of curvature of the beam's wavefront at z and $w(z)$ the evolving beam radius at which the field strength falls to $1/e$ of the axial value, or the beam intensity falls in to $1/e^2$ of the axial value.

When propagating in free space, a Gaussian beam with wavelength λ is fully characterised by a single parameter $\omega_0 = \omega(z=0)$, known as the *beam waist*. In terms of ω_0, the beam radius and wave front's radius of curvature for any z can be expressed as

$$\begin{aligned} \omega(z) &= \omega_0\sqrt{1+\left(\frac{z}{z_R}\right)^2}, \\ R(z) &= z\left[1+\left(\frac{z}{z_R}\right)^2\right], \end{aligned} \tag{D.3}$$

where z_R, known as the Rayleigh range given by

$$z_R = \frac{\pi\omega_0^2}{\lambda}, \tag{D.4}$$

is the axial distance from the waist at which the beam radius $\omega(z_R)$ is $\sqrt{2}$ larger than ω_0.

D.2 Gaussian Beam Collimation and Focusing

The Rayleigh range Eq. (D.4) can be considered the position where the spot size of the Gaussian beam doubles to its value at the waist. For a fixed wavelength, a smaller beam waist means the beam diverges more quickly. In order to collimate a Gaussian beam with waist ω_0 to a beam with radius ω_0', we can put the beam waist at the focal plane of a collimating lens with focal length f given by

$$\begin{aligned} \omega_0' &= \omega_0 \sqrt{1 + \left(\frac{f}{z_R}\right)^2} \\ &\approx \omega_0 \frac{f}{z_R} \\ &= \frac{f\lambda}{\pi\omega_0}. \end{aligned} \tag{D.5}$$

The approximation is valid since $z_R \ll f$. This formula is also useful for focusing a collimated Gaussian beam, which is the reversed problem of Gaussian beam collimation.

Nomenclature

Physical Constants

$\hbar = h/2\pi$	Reduced Planck constant
e	Elementary charge
c	Speed of light
k_B	Boltzmann constant

Quantum Mechanics

$\|\alpha\rangle$	Coherent state
$\|\alpha, m\rangle$	Displaced number state
$p_{\|\psi\rangle}(n)$	Probability distribution of state $\|\psi\rangle$ in Fock state basis
P_S	Probability for finding the ion in $\|S\rangle$ state
$\hat{H}$	Total Hamiltonian in the Schrödinger picture
$\hat{H}_0, \hat{H}_1$	Free term and interaction term in the total Hamiltonian
$\hat{H}_{I,1}$	Interaction term in the interaction picture

Quantum Optics and Trapped Ion Physics

$j \in \{1, 2, 3\}$	Motional mode index
s	Sideband index
Ω_0	On-resonance Rabi frequency for the carrier transition
Ω	Rabi frequency for the carrier transition
$\Omega_{n,n+s}$	Rabi frequency for the sideband transition
δ	Laser detuning
η	Lamb-Dicke parameter

$g_{s,n}(\eta)$	Franck-Condon coefficient

Trapping Potential Engineering

$\Phi_{\text{tot, DC, RF, PS}}(\boldsymbol{r})$	Total, DC, RF and Pseudo Potential
$\mathbf{E}(\boldsymbol{r})$	Electric Field
$\mathbf{H}(\boldsymbol{r})$	Hessian matrix

Laser Physics

$\boldsymbol{E}(t, \boldsymbol{r})$	Electric field
$\boldsymbol{\epsilon}$	Polarisation unit vector
ω_L	Laser's angular frequency
λ	Wavelength
$\boldsymbol{k}$	Wave vector

Mathematical Symbols

$L_n(x), L_n^{\alpha}(x)$	Laguerre polynomials and enerlised Laguerre polynomials
J_α, Y_α	Bessel functions of the first kind and the second kind
$L(x; x_0, \Gamma)$	Normalised Lorentzian function
σ	Standard error
$B(n, p)$	Binominal Distribution
$\|\boldsymbol{x}\|_p$	ℓ_p norm of vector $\boldsymbol{x}$

Acronyms

AC Alternating Current.

AWG Arbitary Waveform Generator.

BBM Break Before Make.

BSB Blue Sideband.

CW Continuous-Wave.

DC Direct Current.

DP Dipole.

DPG Digital Pulse Generator.

FEM Finite Element Method.

FWHM Full Width Half Maximum.

HWP Half Wave Plate.

ID Inner Diameter.

MBB Make Before Break.

MFD Mode Field Diameter.

MMC MicroMotion Compensation.

MSIA Micromotion Single Ion Addressing.

OD Outer Diameter.

PBS Polarised Beam Splitter.

PCB Printed Circuit Board.

PCF Photonic-crystal Fibre.

PI Photoionization.

PMT Photomultiplier Tube.

PS Pseudo-Potential.

QHO Quantum Harmonic Oscillator.

QP Qudrupole.

QWP Quarter Wave Plate.

RSB Red Sideband.

s.e.m. Standard Error of the Mean.

SET Surface-Electrode Trap.

TIQI Trapped Ion Quantum Information.

TOF Time-of-Flight.

TTL Transistor-Transistor Logic.

UHV Ultra High Vacuum.

Bibliography

[Alonso13] J Alonso et al. “Quantum control of the motional states of trapped ions through fast switching of trapping potentials”. *New J. Phys.* 15.2 (Feb. 2013), p. 023001. arXiv: 1208.3986.

[Alonso16] J. Alonso et al. “Generation of large coherent states by bang-bang control of a trapped-ion oscillator”. *Nat. Commun.* 7 (Apr. 2016), p. 11243.

[Berkeland98] D. J. Berkeland et al. “Minimization of ion micromotion in a Paul trap”. *J. Appl. Phys.* 83.10 (Apr. 1998), pp. 5025–5033. arXiv: 1211.0101.

[Bermudez17] Alejandro Bermudez et al. “Micromotion-enabled improvement of quantum logic gates with trapped ions” (May 2017). arXiv: 1705.02456.

[Bevington03] Philip Raymond Bevington and D. Keith. Robinson. *Data Reduction and Error Analysis for the Physical Sciences, 3rd edn.* 2003.

[Boiteux73] M Boiteux and A Levelut. “Semicoherent states”. *J. Phys. A Gen. Phys.* 6.5 (May 1973), pp. 589–596.

[Chiaverini05] J. Chiaverini et al. “Surface-Electrode Architecture for Ion-Trap Quantum Information Processing” (Jan. 2005). arXiv: 0501147 [quant-ph].

[Clercq16a] L. E. de Clercq et al. “Estimation of a general time-dependent Hamiltonian for a single qubit”. en. *Nat. Commun.* 7 (Apr. 2016), p. 11218.

[Clercq16b] Ludwig E. de Clercq et al. “Parallel Transport Quantum Logic Gates with Trapped Ions”. *Phys. Rev. Lett.* 116.8 (Feb. 2016), p. 080502.

[Deslaurier06] L. Deslauriers et al. “Scaling and suppression of anomalous heating in ion traps”. *Phys. Rev. Lett.* 97.10 (Sept. 2006), p. 103007. arXiv: 0602003 [quant-ph].

[Feynman82] Richard P Feynman. “Simulating Physics with Computers”. *Int. J. Theor. Phys.* 21.6/7 (1982).

[Guggemos15] M. Guggemos et al. “Sympathetic cooling and detection of a hot trapped ion by a cold one”. *New J. Phys.* 17.10 (Sept. 2015), p. 103001. arXiv: 1507.07761.

[Hendricks07] R.J. Hendricks et al. “An all-optical ion-loading technique for scalable microtrap architectures”. *Appl. Phys. B* 88.4 (Sept. 2007), pp. 507–513.

[Itano93] W. M. Itano et al. “Quantum projection noise: Population fluctuations in two-level systems”. *Phys. Rev. A* 47.5 (May 1993), pp. 3554–3570.

[Kienzler15] D Kienzler et al. “Quantum harmonic oscillator state synthesis by reservoir engineering”. *Science (80-.).* 347.6217 (Jan. 2015), pp. 53–56. arXiv: 1409.3032.

[Leibfried03] D. Leibfried et al. “Quantum dynamics of single trapped ions”. *Rev. Mod. Phys.* 75.1 (2003), pp. 281–324.

[Leibrandt07] David R Leibrandt et al. “Laser ablation loading of a surface-electrode ion trap”. *Phys. Rev. A - At. Mol. Opt. Phys.* 76.5 (2007). arXiv: 0706.3374.

[Leupold16] Florian M. Leupold. “Bang-bang Control of a Trapped-Ion Oscillator”. PhD thesis. 2016.

[Lo16] Hsiang-Yu Lo. “Creation of Squeezed Schrödinger’s Cat States in a Mixed-Species Ion Trap”. PhD thesis. 2016.

[Lucas04] D. M. Lucas et al. “Isotope-selective photoionization for calcium ion trapping”. *Phys. Rev. A - At. Mol. Opt. Phys.* 69.1 (Oct. 2004), p. 13. arXiv: 0310044 [physics].

[McLachlan64] N.W. McLachlan. *Theory and application of Mathieu functions*. New York: Dover, 1964.

[Navon13] Nir Navon et al. “Addressing two-level systems variably coupled to an oscillating field”. *Phys. Rev. Lett.* 111.7 (Aug. 2013), p. 073001. arXiv: arXiv:1210.7336v3.

[Nazarov03] Yuli V. Nazarov, ed. *Quantum Noise in Mesoscopic Physics*. Dordrecht: Springer Netherlands, 2003. ISBN: 978-1-4020-1240-2.

[Nicholson83] Dwight R Nicholson. *Introduction to plasma theory*. Wiley, 1983. ISBN: 0-471-09045-X.

[Nielsen11] Michael A. Nielsen and Issac L. Chuang. “Quantum Computation and Quantum Information” (2011), p. 702.

[Nieto97] Michael Martin Nieto. “Displaced and squeezed number states”. *Phys. Lett. Sect. A Gen. At. Solid State Phys.* 229.3 (Dec. 1997), pp. 135–143. arXiv: 9612050 [quant-ph].

[Paul53] Wolfgang Paul and Helmut Steinwedel. “Ein neues Massenspektrometer ohne Magnetfeld”. *Zeitschrift für Naturforsch. A* 8.7 (1953), pp. 448–450.

[Paul90] Wolfgang Paul. “Electromagnetic traps for charged and neutral particles”. *Rev. Mod. Phys.* 62.3 (July 1990), pp. 531–540.

[Šašura02] MAREK Šašura and Vladimír BUŽEK. “Cold trapped ions as quantum information processors”. *J. Mod. Opt.* 49.10 (Aug. 2002), pp. 1593–1647. arXiv: 0112041 [quant-ph].

[Schmied] Roman Schmied. *SurfacePattern: a Mathematica package for surface atom and ion traps*.

[Schmied09] Roman Schmied, Janus H. Wesenberg, and Dietrich Leibfried. "Optimal Surface-Electrode Trap Lattices for Quantum Simulation with Trapped Ions". *Phys. Rev. Lett.* 102.23 (June 2009), p. 233002.

[Shor95] Peter W. Shor. "Polynomial-Time Algorithms for Prime Factorization and Discrete Logarithms on a Quantum Computer". *SIAM J. Comput.* 26.5 (Oct. 1995), pp. 1484–1509. arXiv: 9508027 [quant-ph].

[Siegman86] A. E. Siegman. *Lasers*. University Science Books, 1986, p. 1283. ISBN: 0935702113.

[Turchette00] Q. A. Turchette et al. "Heating of trapped ions from the quantum ground state". *Phys. Rev. A - At. Mol. Opt. Phys.* 61.6 (Feb. 2000), p. 8. arXiv: 0002040 [quant-ph].

[Wahnschaff16] Martina Wahnschaffe. "Engineered microwave control for trapped ions". PhD thesis. 2016.

[Wineland13] David J. Wineland. "Nobel Lecture: Superposition, entanglement, and raising Schrödinger's cat". *Rev. Mod. Phys.* 85.3 (July 2013), pp. 1103–1114.

[Wineland79] D. J. Wineland and Wayne M. Itano. "Laser cooling of atoms". *Phys. Rev. A* 20.4 (Oct. 1979), pp. 1521–1540. arXiv: arXiv:1011.1669v3.

Eidgenössische Technische Hochschule Zürich
Swiss Federal Institute of Technology Zurich

Declaration of originality

The signed declaration of originality is a component of every semester paper, Bachelor's thesis, Master's thesis and any other degree paper undertaken during the course of studies, including the respective electronic versions.

Lecturers may also require a declaration of originality for other written papers compiled for their courses.

I hereby confirm that I am the sole author of the written work here enclosed and that I have compiled it in my own words. Parts excepted are corrections of form and content by the supervisor.

Title of work (in block letters):

Motional State Control and Ablation Loading in a Cryogenic Surface-Electrode Trap

Authored by (in block letters):

For papers written by groups the names of all authors are required.

Name(s):	**First name(s):**
Zhou	Peng

With my signature I confirm that

- I have committed none of the forms of plagiarism described in the 'Citation etiquette' information sheet.
- I have documented all methods, data and processes truthfully.
- I have not manipulated any data.
- I have mentioned all persons who were significant facilitators of the work.

I am aware that the work may be screened electronically for plagiarism.

Place, date	**Signature(s)**
Zürich, 31.05.2018	周鹏

For papers written by groups the names of all authors are required. Their signatures collectively guarantee the entire content of the written paper.